NIPER/BDM–0176

Topical Report

MAGNETIC RESONANCE IMAGING TECHNIQUES APPLIED TO THE STUDY OF FLUIDS IN POROUS MEDIA: MAGNETIC RESONANCE MICROSCOPY

by

Daryl Doughty and Liviu Tomutsa

September 1995

Work Performed Under Contract No.
DE-AC22-94PC91008

Prepared for
Dr. Robert Lemmon, Program Manager
U.S. Department of Energy
Bartlesville Project Office

NIPER/BDM–0176
Distribution Categories UC-122 and 125
September 1995

Topical Report

MAGNETIC RESONANCE IMAGING TECHNIQUES APPLIED TO THE STUDY OF FLUIDS IN POROUS MEDIA: MAGNETIC RESONANCE MICROSCOPY

by

Daryl Doughty and Liviu Tomutsa

Work Performed Under Contract No.
DE-AC22-94PC91008

Prepared for
Dr. Robert Lemmon, Program Manager
U.S. Department of Energy
Bartlesville Project Office

BDM-Oklahoma, Inc.
P.O. Box 2565
Bartlesville, Oklahoma 74005

TABLE OF CONTENTS

FIGURES

1.0 INTRODUCTION

Magnetic resonance imaging (MRI) is a nondestructive technology used to image fluids within cores. MRI permits the direct visualization of fluid distributions within the cores without interference from the rock matrix, providing information about porosity distribution and how it is affected by rock heterogeneities. Magnetic resonance (MR) microscopy provides information about the pore network connectivity, which is directly related to fluid flow characteristics within the rock matrix. Such information is important in the development of scaleup procedures from core plugs to whole cores that can be used to verify fluid flow simulations at laboratory scale. The high resolution achievable allows visualization of the effect of rock/fluid interaction on oil, water, and gas distributions within pore spaces of reservoir rocks. Such a capability aids in understanding oil displacement processes taking place at the pore level and is essential in understanding the mechanisms of various oil recovery processes. This report summarizes NIPER's development of MR microscopy to date and its application to the study of multiphase fluid distributions within cores at pore scale. Included in the report are brief descriptions of sample handling techniques and data processing and analysis software developed at NIPER that may be useful to other researchers. The software source code will be provided to interested parties.

A commercial high-resolution Fourier Transform MR spectrometer, modified to be used as an imaging instrument, has permitted the achievement of leading edge MRI developments in (a) resolution, (b) image processing, and (c) distinguishing oil and water phases (Doughty, et al. 1993; Tomutsa, et al. 1992; Doughty and Tomutsa, 1992; Mahmood, et al. 1990; Doughty and Maerefat, 1989; Doughty and Maerefat, 1988; Doughty and Maerefat, 1987). A maximum image resolution of 10 μm is possible based on the high field, the small bore of the spectrometer's superconducting magnet, and other instrument characteristics. By comparison, MRI instruments used for medical purposes generally have about 500-μm resolution. Previous resolution limitations have been overcome by interfacing two high-speed desktop computers with the MR spectrometer. One controls the image data acquisition process in conjunction with the pulse programmer from the spectrometer by controlling the currents in the high-magnetic field gradient coils and acquiring the image data using a high-speed 2-channel AD converter with the recently built sample probe. The other, which also contains an i860 RISC processor (Number Smasher, Microway, Inc.) performs all the computations necessary to generate the fluid image, thus reducing the total time for data acquisition and data processing. The NIPER MR instrument has already been used to generate three-dimensional (3D) images of fluids in cores and beadpacks with resolutions as high as 40 and 25 μm, respectively. The most recent results include imaging of fluid distributions at pore level in Class I reservoir rock types.

The high-resolution MRI microscopy was recently expanded to include multinuclear imaging for direct imaging of separate fluid phases using fluids tagged by an MR-active marker, such as Fluorine-19 (19F). Such an approach can be expanded to image chemical gels, polymers, gas floods, and microbial systems in fractured cores and study effects of fracture systems on chemical trapping. These components, typically present in low concentrations, would be lost in the background unless tagged by an MR-active marker (such as 19F or other sensitive tags) and imaged separately by multinuclear MRI.

In this report, Sections 2.0 to 5.0 summarize recent advances in MRI research at NIPER. Advances in computed tomography and other related research are reported in the Appendix.

2.0 PORE-SCALE MRI HARDWARE AND SOFTWARE

There are several different techniques for acquiring 3D images with MRI equipment, each with its own hardware and software requirements: (1) slice imaging sequences in which successive slices of controlled thickness are captured; (2) 3D fast Fourier transform imaging (FFT) in which two-phase gradients are stepped in value to map 3D image space; and (3) 3D projection reconstruction imaging in which a constant magnitude gradient is stepped through different directions to map 3D image space. These image techniques are also listed in the order of decreasing complexity and length of the pulse sequence required to acquire each image element.

In early efforts at NIPER to develop MRI, the emphasis was on using the existing MR instrument capability to control the data acquisition and processing, particularly using the two-dimensional (2D) capabilities of the JEOL MR spectrometer. The spectrometer imaging interface board was designed to control the imaging gradient amplitudes and timing using gate signals from the spectrometer pulse programmer. An arbitrary waveform generator was used to shape the RF pulses from the spectrometer to achieve a narrow RF bandwidth for thin slice resolution. The spectrometer frequency synthesizer was modified to provide smaller frequency offsets during the RF pulses to control slice position during imaging. An instrument software (PEGS) was available on the spectrometer to write code to design the data acquisition using the pulse programmer. The imaging sequence used was the spinwarp process to acquire data representing a 2D slice through the sample (Dumoulin, 1987). The image data was acquired by the spectrometer hardware directly into the spectrometer acquisition computer for processing.

This approach has proven successful in the biological and medical fields, but is severely limited by the short T_2 relaxation time of fluids in typical porous rock. The spinwarp process, shown schematically in Figure 2–1, required fast sequential switching of imaging gradients, shaped RF pulses to control slice thickness, and needed several ms between RF pulses and signal acquisition. A premium is placed on the rapid switching of the magnetic field gradients and coil designs using shielded gradient coils with short rise and fall times were required. Only fluids in the largest pores in clean porous rock gave sufficient signal to appear in the image. Since the T_2 relaxation time became shorter as the MR magnetic field became higher, successful slice imaging of fluids in rock was accomplished by reducing the magnetic field and running the instrument at 60 MHz instead of the normal 270 MHz. This severely curtailed the use of the spectrometer for high-resolution studies however, so this approach was soon abandoned.

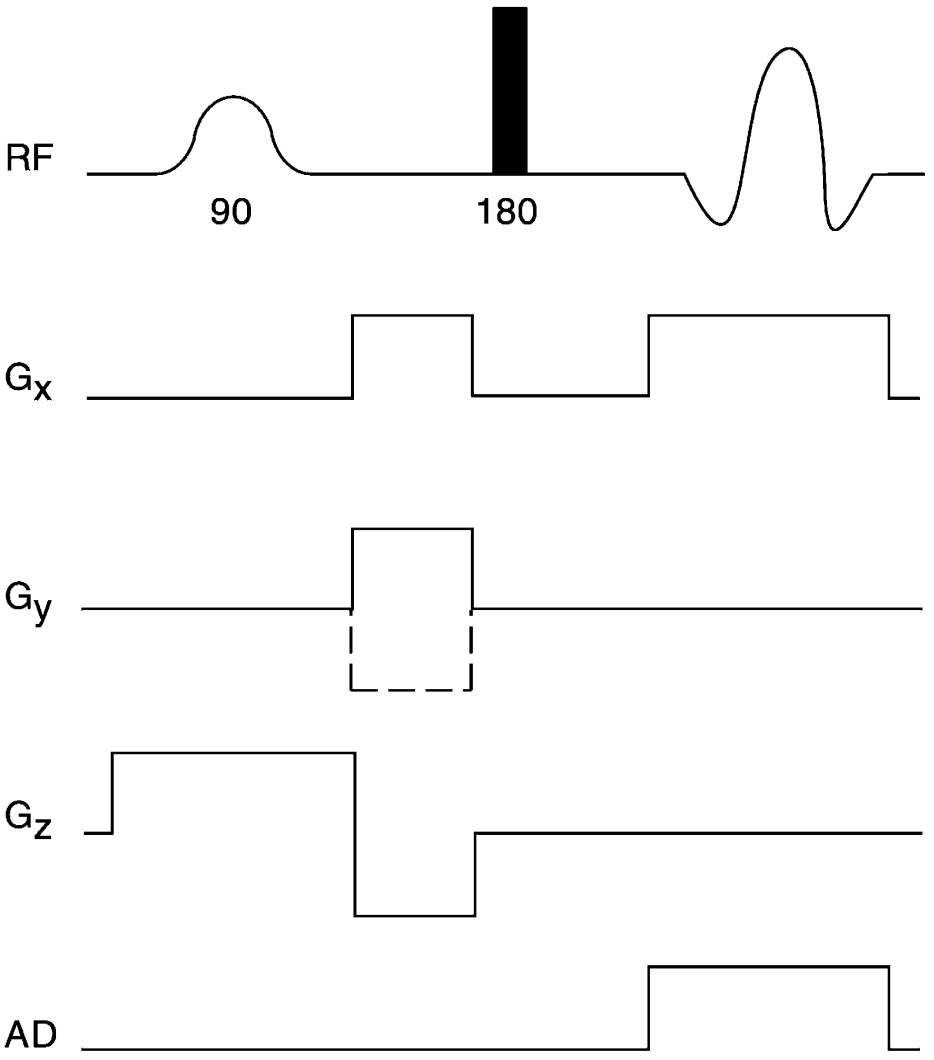

Figure 2–1 Spinwarp MRI Pulse Sequence Using a Spin Echo RF Pulse Sequence with a Shaped 90° Pulse for Slice Selection and a Strong 180° RF Pulse for Inversion to Form the Echo Signal Acquired by the AD Board. The horizontal dimension represents time.

The spinwarp image acquisition sequence encodes the 2D image data in the X-direction using the X-gradient during the signal acquisition and in the Y-direction by stepping the Y-gradient through a sequence of values during the time interval between the 90° and 180° RF pulses as shown in Figure 2–1. The slice thickness is controlled by the length of the RF pulse and the strength of the Z-gradient. This results in a 2D raw data file where the phase of the acquired signal varies from the center of the 2D data set in a Cartesian manner, which is entirely analogous to the data set for a standard 2D high-resolution MR spectrum. Therefore, the image processing can use the existing 2D FFT image processing software that is part of the standard package on the spectrometer. The resulting image represents a cross-sectional XY slice of the

fluid distribution within the sample with the thickness of the slice determined by the Z-gradient strength.

Three-dimensional FFT MRI sequences are less complicated than the spinwarp slice imaging sequence described above (Robinson and Deans, 1991). No slice selection step, which involves a relatively long, narrow-band shaped radio frequency (RF) pulse, is required. This shortens the length of the spin echo imaging sequence, eliminates some complexity in the hardware for pulse shaping, and leads to higher signal-to-noise ratios. The standard 3D fast fourier transform (FFT) imaging sequence still places a premium on fast gradient switching to acquire the imaging data set, as shown in Figure 2–2. The digital-to-analog (DA) output board, which supplies the three X-, Y-, and Z-gradient values to the gradient coils, was modified so the three gradient signals could be shaped with a pre- and post-gradient component. The gradient pulse has a finite rise and fall time controlled by electrical, material, and mechanical factors in the gradient coil, RF probe, and MR magnet assembly. By using a pre-gradient pulse value twice as large and reducing it to the desired value at a time equal to half the coil rise time, the apparent rise time can be reduced to half its actual value. The same principal applies to the post-gradient pulse, which reverses the gradient signal to effectively damp the gradient in half the time. This process can shorten total pulse sequence times by several ms. Because the RF pulses occur in the absence of the gradients, they are not required to irradiate a wide frequency bandwidth and can have lower power levels. The pulse sequence uses the standard spin echo with the fixed amplitude read gradient in the X direction. The Y-gradient is stepped through a sequence of values for each of a set of values of the Z-gradient. This results in a large data file if many steps in the Y- and Z-gradients are used to obtain high voxel resolution. Since the spectrometer software did not provide for 3D FFT data processing, a modified data acquisition program was written to provide the pre- and post-gradient pulse values to the gradient pulses and provide the proper timing relationships between the RF pulses, gradient pulses, and signal acquisition trigger for acquiring the image data. A high-speed, 2-channel, analog-to-digital (AD) converter accessory was used to input the image data to the PC.

The 3D FFT image acquisition sequence encoding for 3D image data is similar to that described for the Spinwarp process for the X- and Y-directions. The difference is no slice selective-shaped pulse with a fixed Z-gradient is used to restrict dimension in the Z-direction. Instead, the Z-gradient itself is stepped through a range of values to define a frequency band of interest. The data set resulting from this process is a nominal complex (real, imaginary) 3D FFT data set that can be processed by any standard 3D implementation of the FFT. The final stage of data processing is to convert the complex data to a magnitude transform for display. A new computer program was written to process the 3D-FFT image data file and recover the image. Use of this 3D FFT processing proved to be 2–5 times faster than processing an equivalent 3D projection reconstruction image data file.

The most efficient 3D imaging process for fluids in porous rock is the 3D projection reconstruction sequence shown in Figure 2–3 (Doughty and Tomutsa, 1992). The imaging gradient is of fixed amplitude and its direction in space is controlled by the three X-, Y-, and Z-components. Since the gradient is switched on prior to the RF pulses in the spin echo. and remains on until the signal is acquired, rapid switching of the gradient is not required and the echo time can be shorter, maximizing signal strength. Achieving high resolutions requires strong gradients and high RF bandwidths. A high field gradient coil assembly was constructed to provide the strong gradients. A high-power RF amplifier was used to provide the short RF pulses and the high-speed 2-channel AD converter was used to acquire the imaging data. Figure 2–4 shows a flowchart of the software developed at NIPER for the acquisition and processing of the projection reconstruction image data.

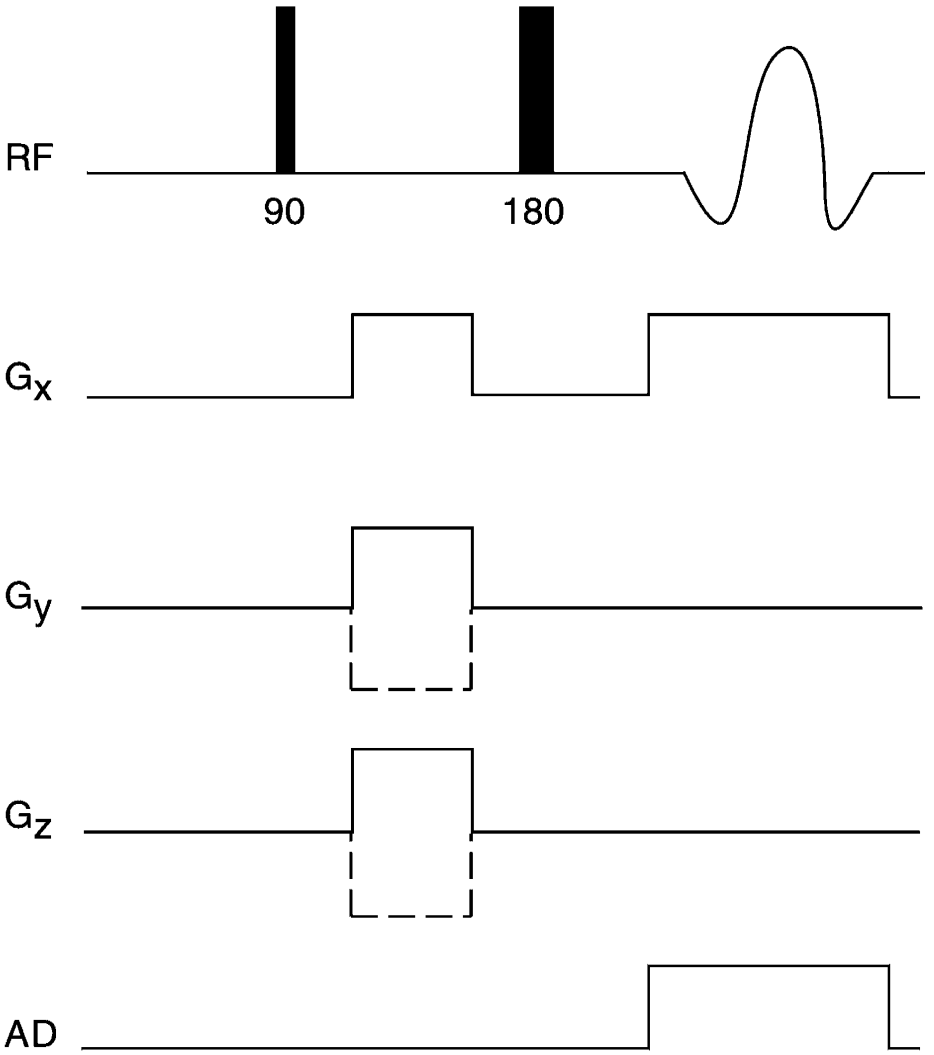

Figure 2–2 Three-Dimensional FFT MRI Pulse Sequence Using a Spin Echo RF Pulse Sequence with Strong 90° and 180° RF Pulses to Form the Echo Signal Acquired by the AD Board. The horizontal dimension represents time.

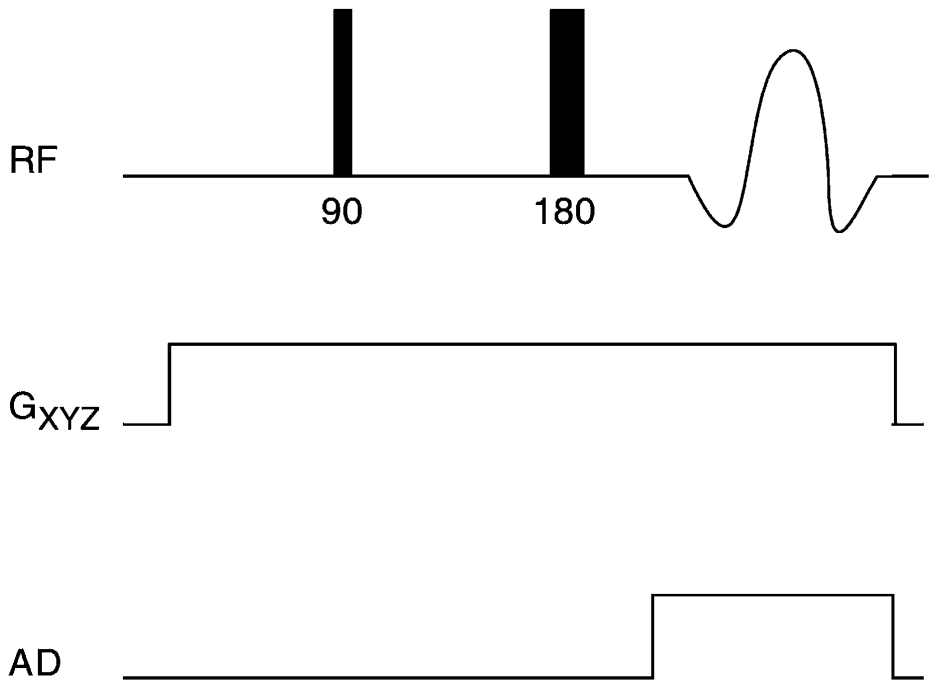

Figure 2–3 Projection Reconstruction MR Imaging Pulse Sequence Using a Spin Echo RF Pulse Sequence with Strong 90° and 180° RF Pulses to Form the Echo Signal Acquired by the AD Board. The horizontal dimension represents time.

The program PRACQGRD (written in C) controls the acquisition of the image data using timing gate pulses provided by the spectrometer pulse programmer, which triggers the switching of gradients and acquisition of the echo signal by the AD converter through the manufacturer-supplied subroutines. PRACQGRD selects the components of the gradient in proper sequence and outputs the amplitudes through a digital/analog converter (subroutine CDA600.ASM) to the gradient amplifiers when triggered by the spectrometer (subroutine CIOWAIT.ASM). The AD converter acquires the echo signal when triggered by the pulse programmer and PRACQGRD downloads the data from the AD converter memory and writes it to the accumulating data file on the PC's hard drive. Because the image acquisition can be lengthy for a 3D experiment, PRACQGRD is set up to acquire the image data in several blocks, with each block being written into a separate file on the hard drive (XXXXXA.DR2, XXXXXB.DR2,...). In case of a power outage during the experiment, which terminates the acquisition, the experiment can then be restarted near the point of interruption without redoing the entire experiment. Also, PRACQGRD writes a parameter file (XXXXX.PAR), which contains the instrument parameters and number of projections used during the experiment.

In the second step, as shown in Figure 2–4, the program FFPOW (written in FORTRAN) uses the FFT contained in subroutine FFTC.F to transform the complex image data into a power transform showing the projection of the spin intensity across the sample for each position of the gradient. Complementary to the acquisition process described above, FFPOW reads the separate raw data files in sequence, transforms them, and welds them into one large projection data file (XXXXX.DP2).

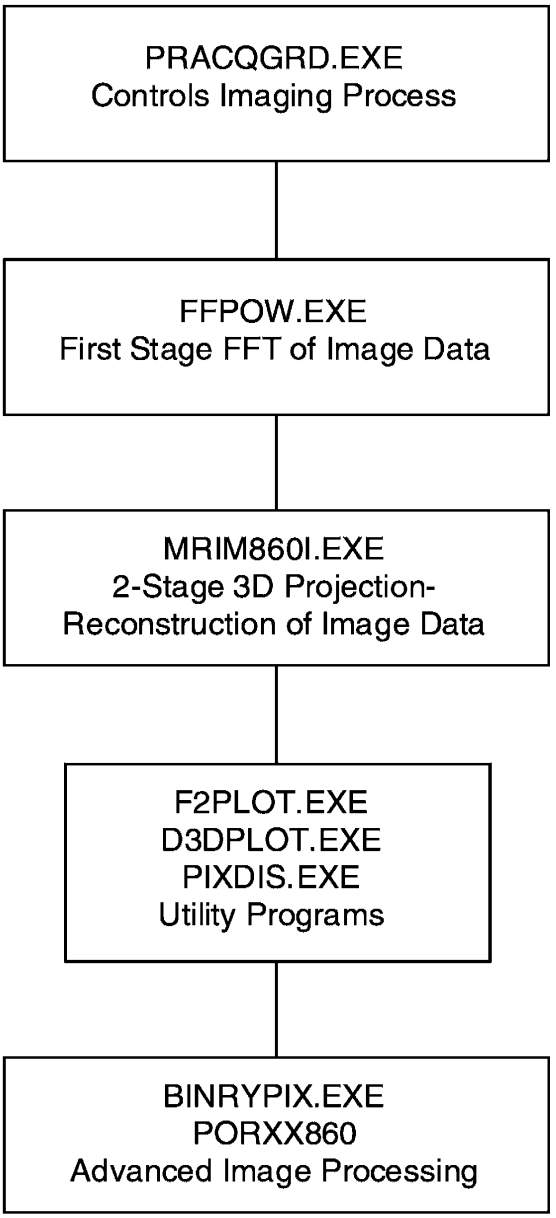

Figure 2–4 Flowchart of Basic Projection-Reconstruction MR Image Acquisition and Data Processing Utilizing Software Developed at NIPER.

The algorithm used to process the projection-reconstruction image data is a two-stage implementation of the convolution method for parallel beam reconstruction tomography from the Donner Laboratory algorithms (Huesman, et al. 1977). In adapting this algorithm for MRI, the MR projection is treated like a parallel beam emission projection of source intensity across the dimension of the object defined by the gradient direction. This implementation is embodied in the program MRIM860I shown in block 3 of Figure 2–4. The main program, MRIM860I.F, reads the input projection data file (XXXXX.DP2 using subroutine GETUM.F) along with user data file parameters, or it can get the input parameters from a parameter input file (MRICM1.PAR). Other subroutines used in the reconstruction process are contained in the source code MCONVO.F and MSETUP.F. The output is a 3D binary data file (XXXXXX.DIC) where each byte represents the voxel intensity on a 0–255 scale. Because of memory restrictions on the Number Smasher board used for image processing, a subset of the complete image is output for larger images (256 x 256 x 120 voxels).

Several utility programs have been written to aid in checking and examining the MR image data files at various stages of acquisition and processing. These programs are highlighted in the fourth block in Figure 2–4 and all are written in FORTRAN. F2PLOT is a program that graphically displays a 512 element record from either the raw image file (XXXXX?.DR2) or the intermediate transformed image file (XXXXX.DP2). It can be used to quickly scan the data files for irregularities arising from possible glitches in the data acquisition process. D3DPLOT is used to display XY slices of the final image file (XXXXXX.DIC). The image is displayed as a grayscale image and multiple successive slices are displayed depending upon the size of the image. This is useful for quickly surveying the final image file and selecting regions of interest for more complete study. Both of these programs use a graphics subroutine library that is specific to the FORTRAN compiler (NDP FORTRAN, Microway, Inc.). PIXDIS is a program that scans through a selected region of the final image file (XXXXXX.DIC) and develops a histogram of voxel intensity. This is useful for selecting a threshold intensity level related to certain physical parameters for the sample, such as fluid-filled porosity.

3.0 CASE STUDIES

3.1 Slice MR Imaging

Figure 3–1 shows two cross-sectional slice images of a brine-saturated Cleveland sandstone core plug. The core plug was 1 inch in diameter and 3 inches in length and saturated with 1% NaCl brine. A 1.024 ms long gaussian RF pulse was used with a 3 gauss/cm Z-gradient giving a slice thickness of 1.6 mm. An X-gradient of 1.9 gauss/cm was used during data acquisition and the Y-gradient was stepped through 256 values from -1.9 gauss/cm to 1.9 gauss/cm. The two images have 256 x 256 pixels for an inplane resolution of about 150 μm/pixel. In 3–1*A*, a time-to-echo (TE) value of 10.4 ms was used in the spinwarp pulse sequence. There are a few regions where the signal intensity is lower, indicating smaller pores or higher clay content in the rock matrix. In 3–1*B*, a longer TE value of 19.4 ms was used to more strongly reduce the intensity of regions having shorter T_2 values from smaller pores or increased clay content.

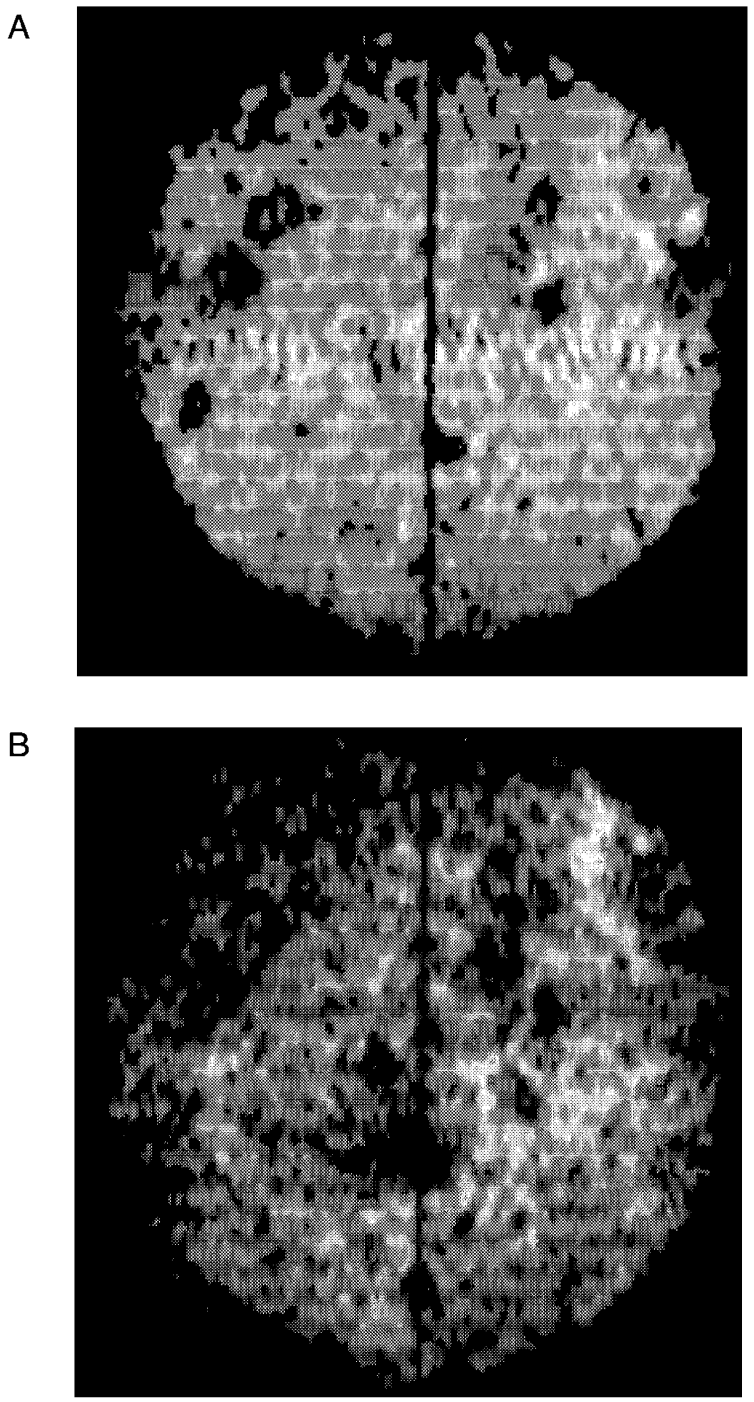

Figure 3–1 **Slice Images of Brine-Saturated Cleveland Sandstone Using Different TE Values to Emphasize Smaller Pores/Higher Clay Content. *A*, TE=10.4 ms; *B*, TE=18.4 ms. Signal intensity from fluid in smaller pores is attenuated at longer TE (shorter T_2).**

3.2 3D FFT MR Imaging

Figure 3–2 shows one cross-sectional slice from a 3D image of an oil-saturated polymer beadpack. The polymer beads ranged in size from 125—1000 μm diameter. The figure shows the oil between the beads in lighter shades with the beads shown as the darker circular areas. The large circular dark area in the lower left quadrant is the silhouette of an air bubble in the beadpack. The beadpack had a diameter of 12.5 mm and the natural line width of the oil signal in the beadpack was 300 Hz. The image has 128 x 128 pixels for a resolution of about 150 μm per pixel. This image was acquired using 128 steps in the Y-gradient and 64 steps in the Z-gradient with 128 complex points in the acquisition of the signal. The shielded gradient coil was used with the standard 15 mm MR probe. The gradient rise times for this combination were about 2 ms, so the pre- and post-gradient pulse periods were set at 1 ms. Total gradient pulse lengths were 5 ms so the TE was about 10 ms. This TE value is about the minimum that can be achieved with our current gradient/probe hardware using the 3D FFT imaging process. Therefore, images of fluids in typical sandstones with shorter T_2 values would be more difficult to obtain using this process.

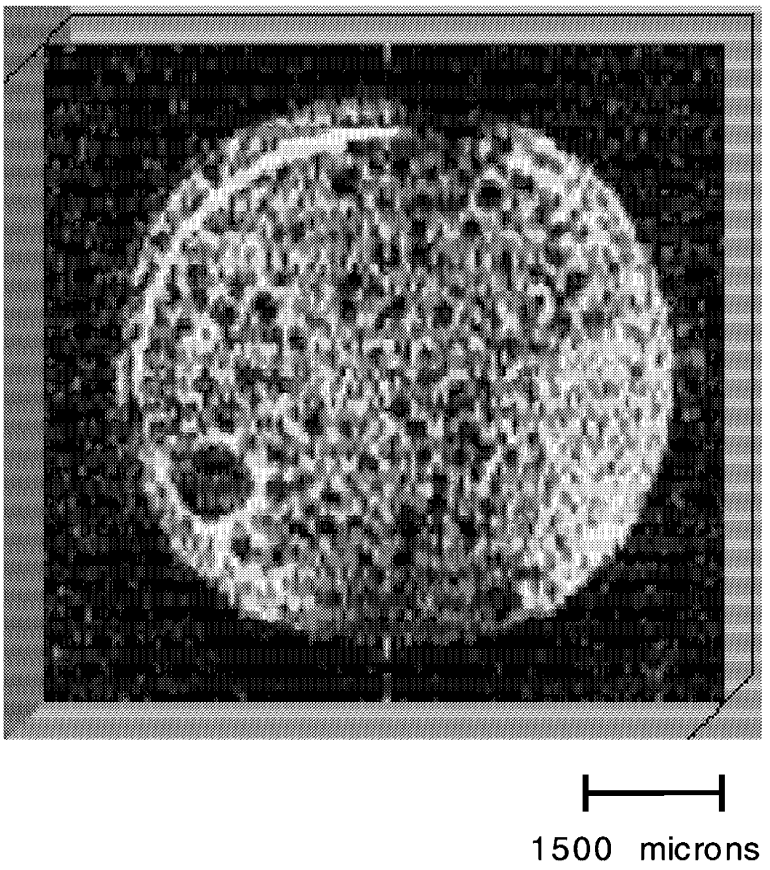

Figure 3–2 Horizontal Slice Through Oil-Saturated Polymer Beadpack. Silhouettes of the beads appear dark; the oil appears white.

3.3 Single-Phase Proton MR Microscopy

A small core plug of Fontainebleau sandstone 5.4 mm in diameter and 7.0 mm long was prepared and mounted in a Teflon shrink tubing core holder developed at NIPER. This core holder consists of two Teflon end caps machined from 1/4 inch diameter Teflon rod as shown in Figure 3–3. The end caps are sealed to the core plug by using a two-layer Teflon shrink tubing system. The first layer is made of FEP Teflon, which shrinks at a temperature of 206°C. The second layer consists of PTFE shrink tubing, which shrinks at a temperature of 320 °C. At this higher temperature, the FEP Teflon inner layer softens and seals tightly to the end caps and core plug, making a tight core holder that contains no protons—which might interfere with the imaging of the fluids in the core plug. The shrink process is controlled by using an electrically heated coil surrounding a piece of 10 mm Pyrex glass tubing that holds the core holder assembly. Lengths of 1/16 inch diameter Teflon tubing are then pushed into the end caps and clamped in place using 2 turns of insulated 22 gauge copper wire twisted about the neck of the endcap. This creates an easily constructed core holder that can be mounted into the imaging probe and placed inside the MR spectrometer magnet. Fluids can be easily introduced into the core plug through the small diameter Teflon tubing without disturbing the position of the core plug in the probe.

MR imaging experiments were done on the core plug saturated with brine containing 0.5% NaCl with 0.02% $MnCl_2$ as a relaxation agent. Measurement of the natural line width of the water MR signal from the brine in the rock gave a result of 750 Hz. An image of the water was obtained using 256 X,Y-gradient steps with 128 Z-gradient steps. The image obtained had a resolution of 30 μm. Slice images from the 3D image data set for the Fontainebleau sandstone revealed the presence of randomly scattered large pores with little porosity in between. A thin section of the sandstone was prepared and computer assisted petrographic image analysis (PIA) measurements showed an average porosity of 12%. An upgrade of the DICER image analysis software permits surface rendering of 3D volumes. Figure 3–4 shows a surface rendering of an isolated large pore from the above data set. The lower intensities corresponding to rock grains and the higher intensities corresponding to bulk water have been made transparent, so only the thin layer of water near the rock grain surface is visible. The irregular shape of the pore volume determined by the surrounding rock grains is apparent, as are several narrow pore throats connecting to other pores outside the volume shown.

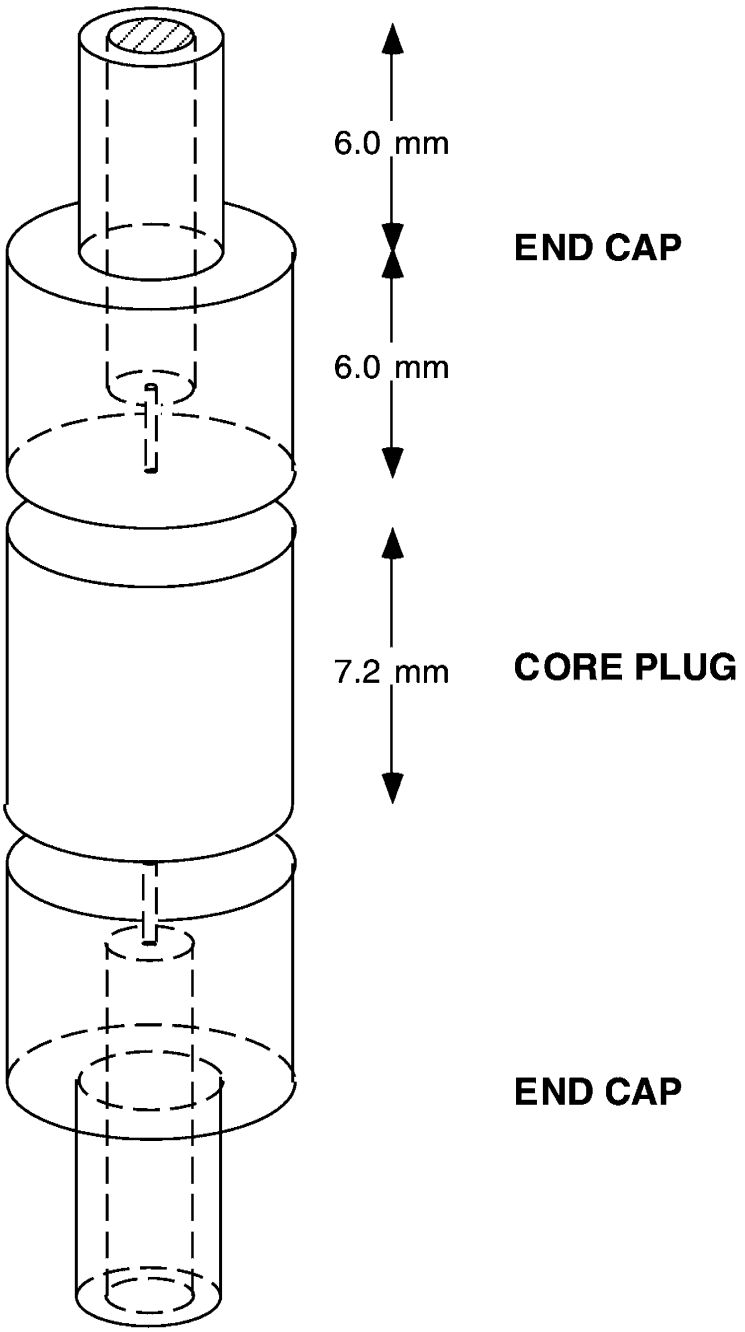

Figure 3–3 **Arrangement of Components in the Core Holder. Teflon end caps are machined from Teflon rod with a 1/16 inch diameter hole for the Teflon tubing. The core plug is typically 7.0 - 10.0 mm long. In actual use, the two end caps are pressed against the faces of the core plug before being encased in the Teflon shrink tubing.**

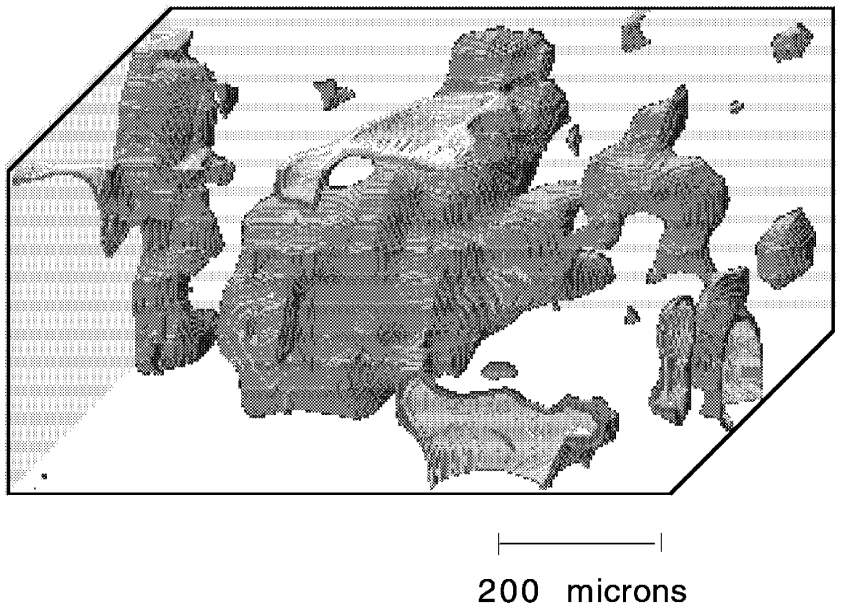

Figure 3–4 **Surface Rendering of Fontainebleau Sandstone Showing the Thin Layer of Water Near the Rock Grain Surface. The rock grains and bulk water have been made transparent.**

3.4 Three-Dimensional Pore Analysis

For advanced image processing two additional programs, BINRYPIX and PORXX860, have been developed as seen in the last block in Figure 2–4. These programs are written in FORTRAN. Three versions of the PORXX860 program are available for input images of 32, 64, and 128 voxels on edge. BINRYPIX accepts as input the XXXXXX.DIC file and converts a specified subregion of the data into a binarized image, where voxels at or above a specified intensity threshold are set to 255 and those below the threshold are set to zero. After the data is binarized, successive 3D erosion/dilation cycles (up to 6) may be performed on the image to break narrow features in the data set connecting adjacent pore spaces and isolate larger pore spaces. This is a true 3D process as adjacent layers above and below the layer of interest are used to guide the erosion/dilation process that uses a 3D kernel (3 x 3 x 3 cross or 4 x 4 x 4 cube with missing corners).

PORXX860 accepts as input the binarized image output by BINRYPIX. The version of PORXX860 must be used that matches the size of the binarized image file (32, 64, or 128 voxels on edge). As PORXX860 scans through successive layers of the image file, a table of pore indices is constructed with accumulated pore volumes as a sum of voxels for each isolated pore identified. In a succeeding layer, if a bridge is found connecting two or more previously isolated pores, then the sum of the volumes are accumulated in the lowest ranking pore index of the connected spaces, and the other pore indices are zeroed and freed for subsequent use. Thus, when the entire volume of the image set is scanned, the table of pore indices will contain one entry for each separately identified pore space with its accumulated volume in voxels. Also, the program develops a table of the X, Y, and Z ranges over which a given pore space extends within the image volume. If a given sample has a well-connected pore system, it is possible for all the discovered pore volume within the image volume to end up in one pore.

The MR microscopy data for the Fontainebleau sandstone/brine system was analyzed for porosity distribution and compared to results obtained from petrographic analysis on the same rock. Measurements of fluid filled porosity showed that the area was significantly influenced by the image pixel intensity threshold used. On this basis, an intensity threshold was selected that gave an average porosity result equal to the average result from PIA. Figure 3–5 indicates that the MR porosity distribution is much narrower than that for PIA. This arises from two reasons: (1) the MR data is obtained from a small sample that is likely to be more homogeneous and (2) the PIA method samples a smaller field of view, that causes larger pores to more strongly influence area measurements at a given location on the thin section. This advanced image processing software was applied to the 3D MRI data file for brine-saturated Bentheim sandstone. Even after erosion/dilation to isolate pores, the 3D pore size software put over 75% of the porosity into one pore, indicating that the pore throats are much larger than those found in the Fontainebleau sandstone.

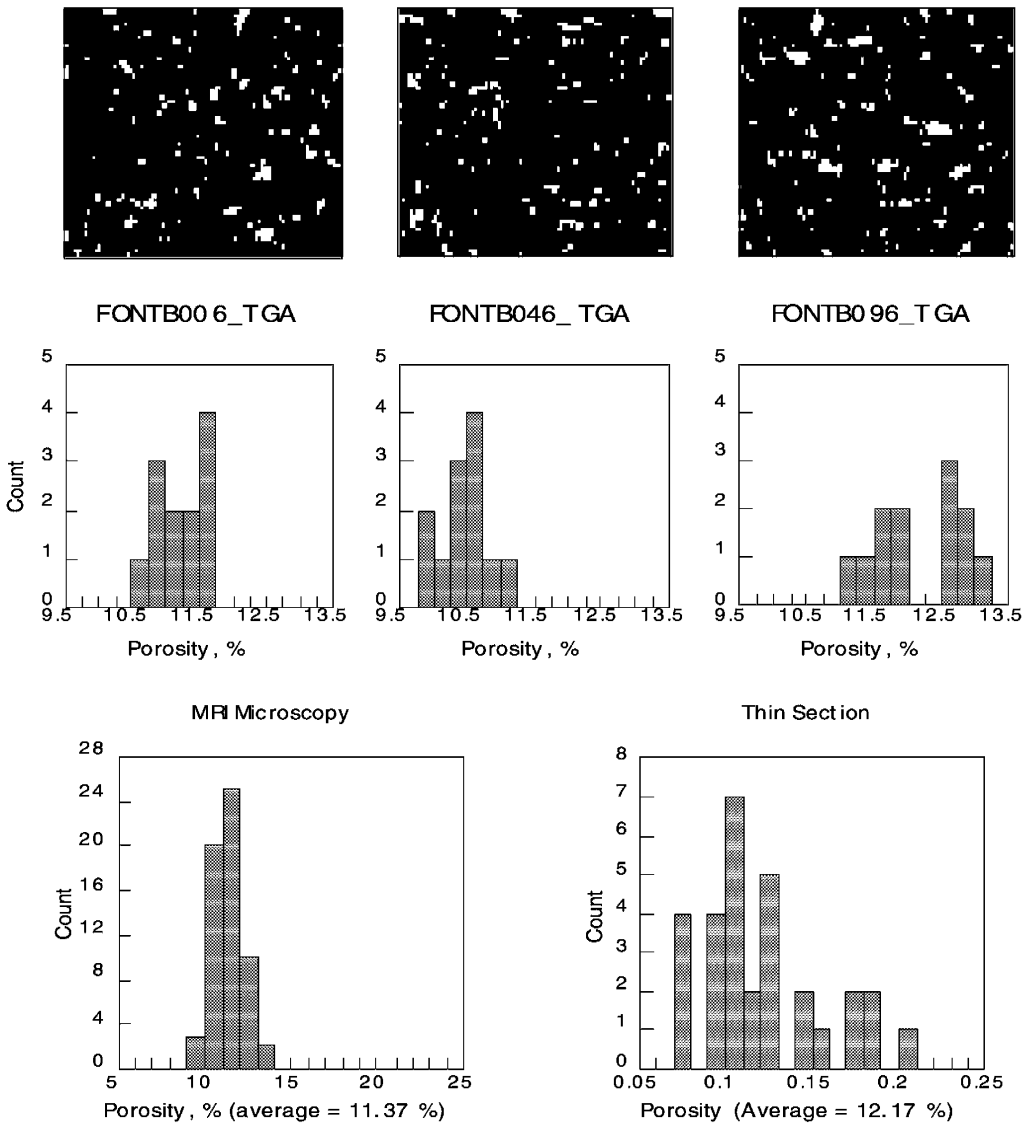

Figure 3–5 **Fontainebleau Sandstone Porosity Distributions from NMRI and PIA are Shown. Two dimensional slices (at positions 6, 46 and 96) taken from the three dimensional data are displayed.**

3.5 Two-Phase Proton MR Microscopy

A small core plug of Fontainebleau sandstone 5.4 mm in diameter and 7.0 mm long was prepared and mounted in a Teflon shrink tubing core holder. The core plug was saturated with 0.5% NaCl brine under vacuum and mounted in the imaging probe. The brine in the core plug contained $MnCl_2$ relaxation agent to shorten the T_1 time for imaging experiments. MR images of the core plug were made for the brine saturated state showing total fluid-filled porosity; the brine/Soltrol-saturated state (5 cps viscosity) at residual brine using longer TE imaging to suppress the brine signal and showing the oil-filled porosity; and the brine/Soltrol-saturated state at residual oil using longer TE. By subtracting the longer TE images from the initial brine saturated image, the brine-filled porosity in the two-phase systems can be displayed. Figure 3–6 shows the two-phase brine/Soltrol fluid-filled porosity for three successive regions down the axis of the core plug. Views *A*, *D*, and *G* show the initial brine-saturated total porosity. The direction of fluid flow in the figure was from *A* to *D* to *G* back to front. Views *B*, *E*, and *H* show the corresponding oil-occupied porosity for the same respective regions and views *C*, *F*, and *I* show the corresponding residual brine-occupied porosity in the three regions. Even though approximately 10 pore volumes of oil was flowed through the core plug before the second experiment was run, Figure 3–6 shows that the relative volume of the total porosity occupied by Soltrol is decreasing and the volume occupied by brine is increasing as the distance from the inlet port increased.

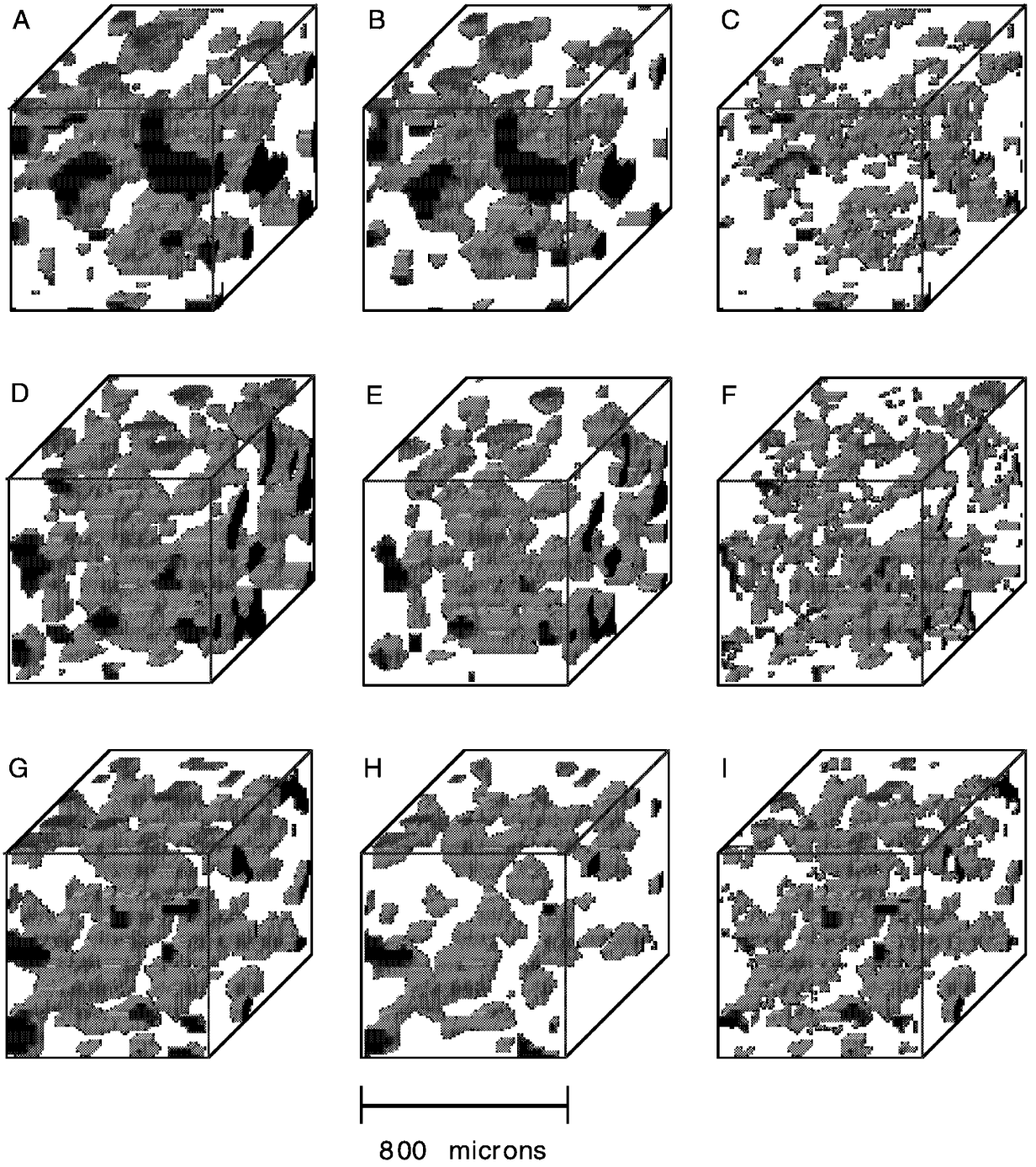

Figure 3–6 **Two-Phase Fluid-Filled Porosity in Fontainebleau Sandstone. *A*, *D*, and G are successive views down the axis of the core plug showing the initial brine saturated total porosity (flow was from back to front in all views; views *B*, *E*, and *H* show the corresponding oil occupied porosity at residual brine; views *C*, *F*, and *I* show the residual brine occupied porosity obtained by difference.**

3.6 Off-Axis Amplitude Attenuation Effect

During the MRI experiments previously discussed, an effect was noticed that impacts on the quality of the images generated in the MRI experiments on two-phase systems. At the longer TE times used to suppress the brine signal for imaging the oil phase, the amplitude of the signal obtained for gradient orientations that were not along the axis of the RF coil (Z direction) or in the X-Y plane were much lower. The magnitude of this effect was related to TE with greater suppression of off axis signal amplitude at longer TE values. To investigate this effect, a phantom sample was made containing both the $NaCl/MnCl_2$ brine and Soltrol as bulk liquid phases inside a small Teflon sample holder approximately 5 mm in diameter and 7 mm long. A series of imaging data acquisitions of varying TEs were run on the phantom using an abbreviated sequence of 16 gradient orientations. Figure 3–7 shows the results for two of the experiments—one at a TE of 1.92 ms (*A*) and the other at a TE of 10.24 ms (*B*). The figure shows the MR projections of the two-phase fluid system in the phantom at the various gradient orientations. Figure 3–7*C* shows the respective gradient orientations for each of the projections shown in *A* and *B*. As is evident in Figure 3–7, at longer TE values the projections at gradient orientations containing both XZ or YZ components are much lower in amplitude.

In the absence of a gradient, the MR signal from the phantom shows the two peaks corresponding to the water signal from the brine and the Soltrol signal. Figure 3–8 shows the relative signal amplitude, expressed as the area under the respective peaks, for the brine and oil phases as a function of TE. The fitted curves were obtained using an exponential function. The brine signal area decreases rapidly with increasing TE because of the relaxation effects of $MnCl_2$, while the oil signal is only slightly affected. The area under the projections in Figure 3–7*A* and 3–7*B* is proportional to the sum of the two peak areas at the corresponding TE values in Figure 3–8. Using the sum of the two peak areas at each TE value from Figure 3–8, each of the imaging experiments was normalized to the signal amplitude at a TE of 0.0 ms. Figure 3–9 shows the results for each of the imaging experiments at TEs from 1.92–10.24 ms with the grayscale intensity showing the normalized signal area at each gradient orientation shown in Figure 3–9*B*. The implication of this for MRI experiments is that the TE used for suppression of the brine signal to get the oil image must not be so long that the off axis signal amplitude is seriously affected. This problem can be avoided altogether by using multinuclear MRI. For example, the oil image could be obtained from a perfluorinated hydrocarbon using 19F MR. A short TE could then be used for both fluids, capturing more of the signal in each case.

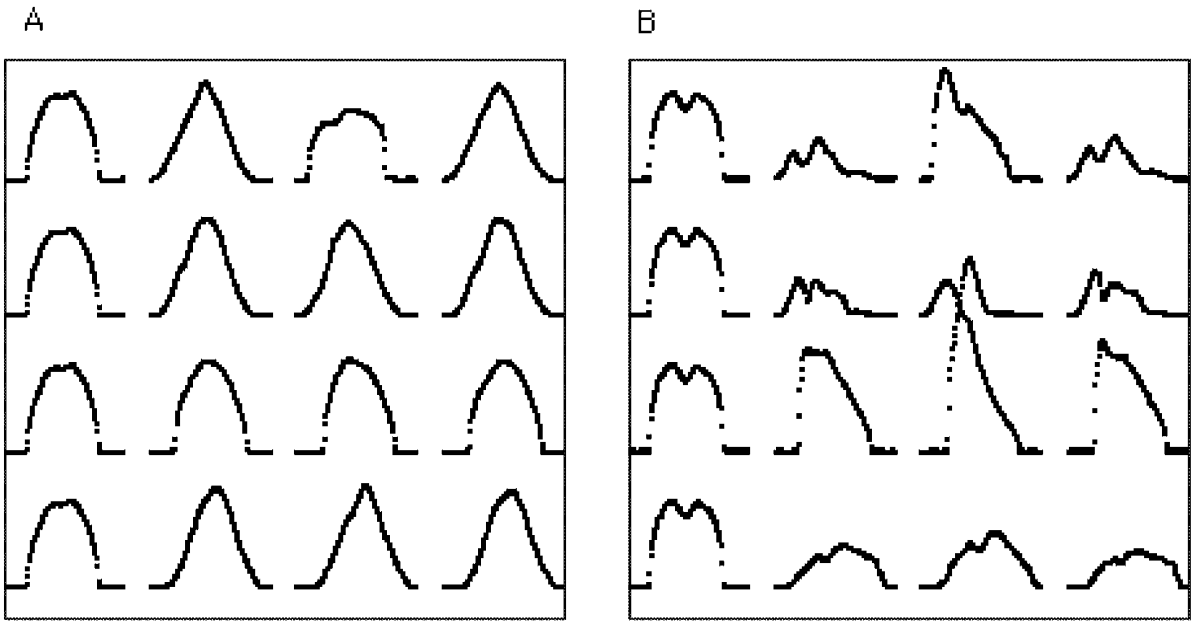

C

X	XZ	Z	-XZ
X	XYZ	YZ	-XYZ
X	XY	Y	-XY
X	-XYZ	-YZ	-XYZ

Figure 3–7 **Experimental Imaging Data Projects for Varying TEs. *A*, MRI echo signal projections for the brine/soltrol phantom at various gradient orientations for a TE of 1.92 ms; *B*, projections for the same gradient orientations at a TE of 10.24 ms; *C*, chart showing the gradient directions for the respective projections in *A* and *B*.**

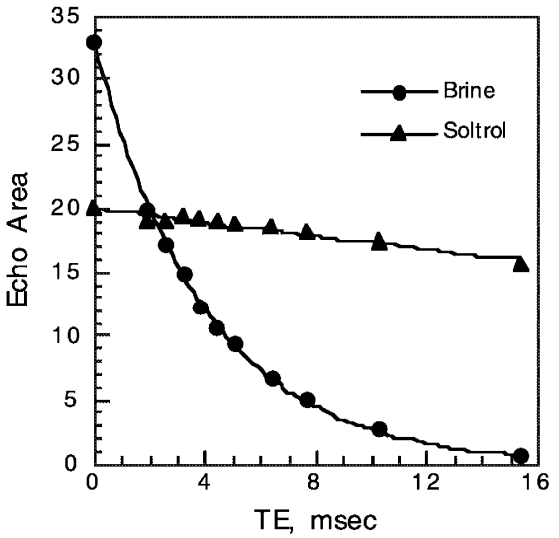

Figure 3–8 **Brine and Soltrol NMR Echo Signal Areas Plotted as a Function of Time-to-Echo (TE) for the Two-Phase Brine/Soltrol Phantom Sample.**

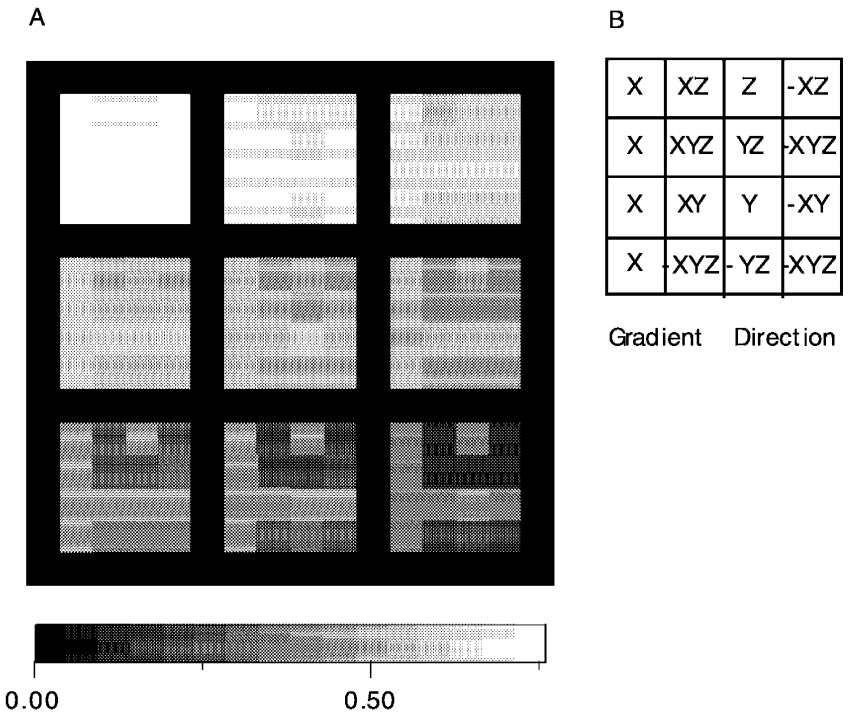

Figure 3–9 **Sets of Normalized MRI Signal Peak Areas as a Function of Gradient Orientation for Increasing TE Values. *A,* Areas under the echo peak are displayed as grayscale intensities for each gradient direction. The TE value for each set increases from left to right and from top to bottom in the figure. *B,* Chart showing the gradient direction for each intensity value displayed in each set in A.**

To further investigate the effects of off-axis gradients on the suppression of MR signals at longer TE values during spin-echo imaging, 2D MRI experiments were performed on a small phantom sample containing either water or cyclohexane. The phantom consisted of a small spherical bulb of 3.2 mm internal diameter completely filled with the fluid of choice. The spherical shape was selected to eliminate any influence of sample geometry on the signal suppression. The two fluids were chosen to see if molecular polarity or shape had any influence on the signal suppression. Imaging experiments were conducted using either 64 or 128 gauss/cm gradient with orientations from 0° to 180° in the XZ plane or the YZ plane at TEs from 5.12 ms to 40.96 ms. In the XZ plane experiments with the water-filled phantom, gradient strengths of 7.45 gauss/cm, 18.6 gauss/cm, or 37.3 gauss/cm were used. In the other experiments, a gradient of 18.6 gauss/cm was used. Also, one experiment was performed in which the phase of the 180° inversion RF pulse was the same as the 90° pulse during the pulse sequence instead of the normal X-Y phase relationship between the 90°–180° pulses.

Figure 3–10 shows the results of the experiments on the water-filled phantom at a TE of 10.24 ms for varying gradients strengths. The area under the MR projection signal was plotted versus the gradient angle index in the XZ plane. The figure shows that the average signal area for all gradient orientations is strongly affected by gradient strength, with the stronger gradient causing a greater suppression of the signal at a given TE. Also, the influence of gradient orientation on the signal is much less pronounced at the weakest gradient of 7.45 gauss/cm. The average suppression of the MR signal in the presence of a gradient is caused by the diffusion of fluid molecules from one location in the sample to a region of a different magnetic field during the TE. Consequently, the contribution of that molecule to the signal strength is missing from the echo signal.

Results from other experiments show similar effects on the MR signal versus gradient orientation when using cyclohexane instead of water; the YZ plane instead of the XZ plane for the gradients; or the X-X phase relationship between the 90°-180° RF pulses The amount of suppression of the echo signal by the gradients is less at a given TE for the cyclohexane than for the water. Since the bigger cyclohexane molecule has a smaller diffusion coefficient than the water molecule, this causes a smaller impact on the echo signal area.

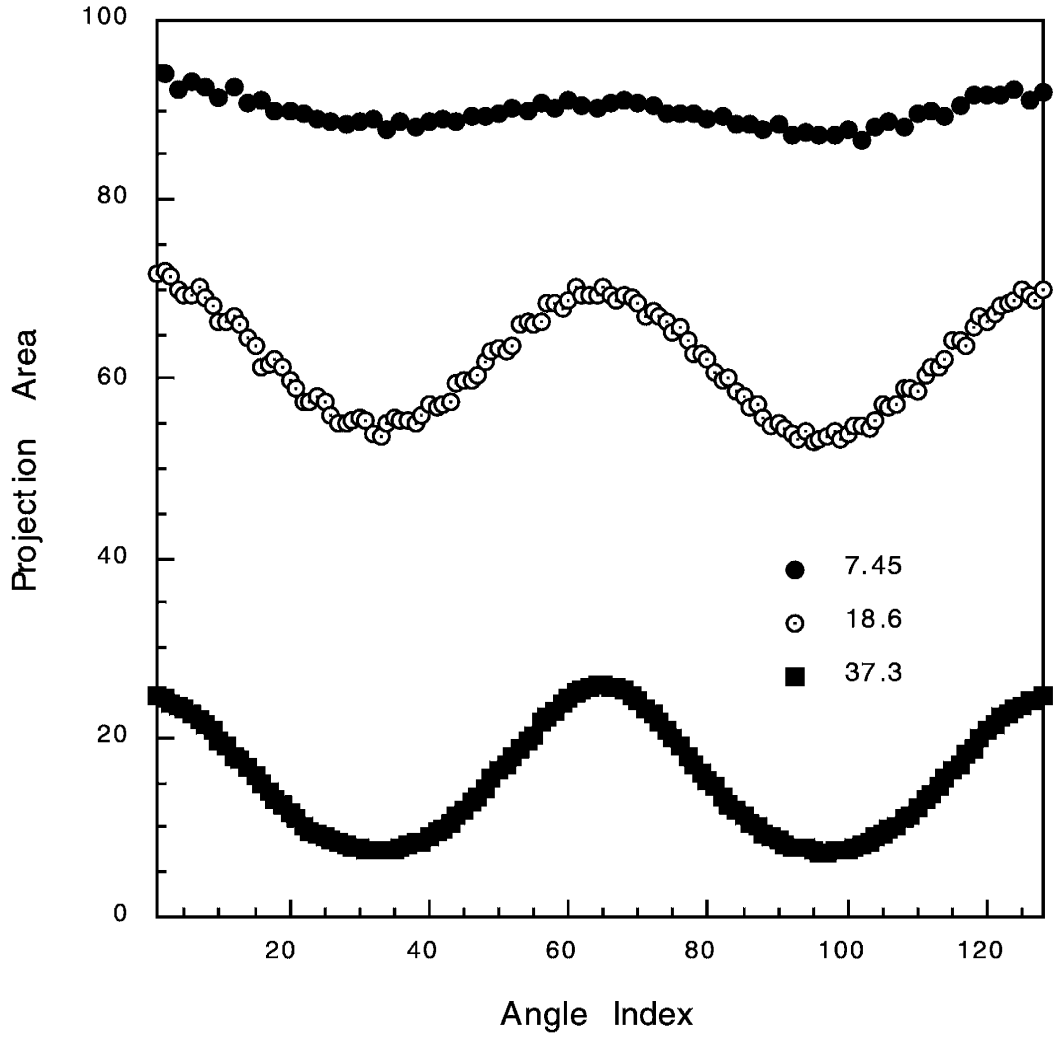

Figure 3–10 **Phantom Projection Areas Plotted as a Function of Angle Index in the XZ Gradient Plane. Data are shown for experiments run at the same TE (10.24 msec) for the three gradient strengths shown in the legend.**

3.7 Multinuclear MR Microscopy

Multinuclear MRI experiments at 19F and proton frequencies were done on a spherical phantom sample containing a mixture of Soltrol and hexafluorobenzene. The resulting images at these two frequencies are identical, except for the size of the image scales with the MR frequency. Proton and 19F MR frequencies are within 6% of each other (270.1 MHz and 254.0 MHz in the 6.34 Tesla magnetic field of NIPER's MR instrument) and can be observed with the same RF coil with suitable tuning capacitors. These tuning modifications were completed for the high-frequency RF coil circuit, and several experiments were made to test the multinuclear imaging capability. Several fluids were available having all the protons on the hydrocarbon structure replaced with

fluorine atoms: a perfluorinated kerosene and hexafluorobenzene. The ideal imaging fluid will have the signal in a single sharp peak or a group of closely spaced peaks. Fluorine MR tests of the perfluorinated kerosene revealed a complicated spectrum containing peaks spread out over 40,000 Hz, and thus unsuitable for imaging. Hexafluorobenzene has a single sharp peak, but also other less desirable qualities such as a relatively low boiling point and viscosity. It was used for these initial experiments while other more suitable chemicals were being ordered.

The imaging probe body contains components near the RF coil that are made of Teflon containing 19F atoms. Figure 3–11 shows two 19F MR spectra of a small glass bulb containing a mixture of Soltrol oil and hexafluorobenzene centered in the RF coil. The first spectrum (A) shows the normal MR spectrum obtained with a single RF pulse, followed immediately by signal acquisition. The sharp peak of the hexafluorobenzene is seen in the center of the spectrum, with a very broad peak at lower frequency coming from the Teflon components of the probe body. This peak is broad because of the strong spin-spin relaxation (T_2) present in a solid. The second spectrum (B) shows the MR spectrum obtained using a spin-echo experiment with a 2.56 millisecond TE. This is a pulse sequence similar to the one used for imaging. Because of the short T_2 time for the solid Teflon signal, it is completely suppressed in the spectrum; only the peak from hexafluorobenzene is seen. This result indicates the solid Teflon components will not interfere with fluid imaging.

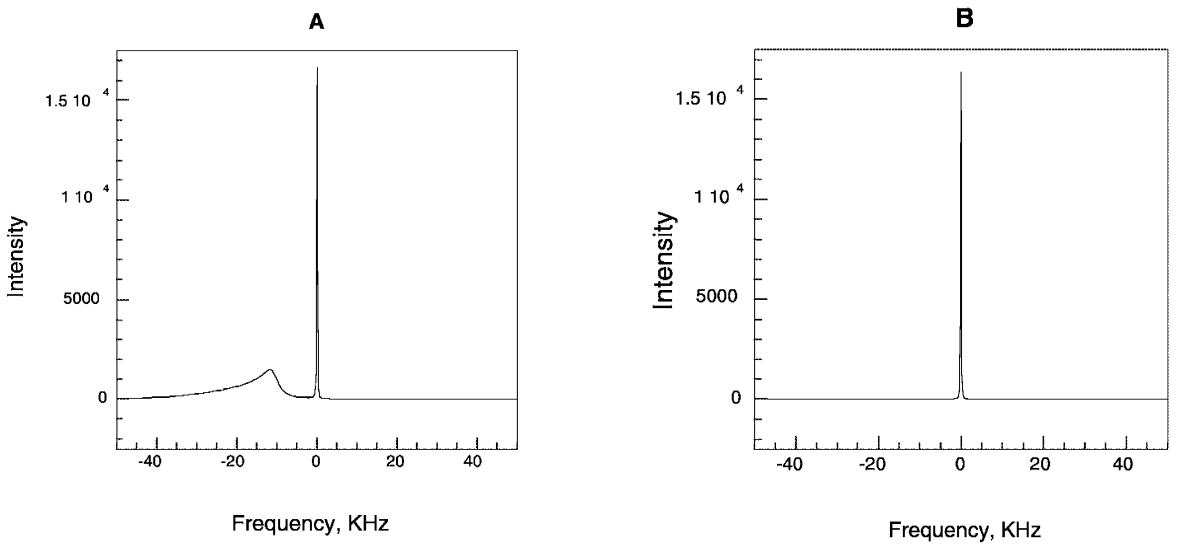

Figure 3–11 Fluorine MR Spectra of a Spherical Glass Bulb Filled With a Mixture of Soltrol and Hexafluorobenzene. *A*, spectrum acquired with single pulse sequence showing broad peak from Teflon in the probe body along with hexafluorobenzene; *B*, spectrum acquired with a spin-echo sequence with 2.56 msec TE showing suppression of the solid Teflon peak.

Figure 3–12 shows the 19F and proton MR images of the spherical glass bulb filled with the two fluids. Figure 3–12*A* shows the 19F image and Figure 3–12*B* shows the proton image. The images were obtained using the same imaging gradient strengths and RF pulse sequences. Measurements show the proton image is larger than the 19F image by the ratio of the proton frequency to the 19F frequency. The glass bulb containing the fluid mixture had an internal diameter of 3.2 mm and the images contain 128 x 128 pixels each. The MR image processing software was modified to correctly scale the 19F image files for the difference in frequency between the 19F and proton MR data acquisition. Figure 3–13 shows the projected MR intensity in the XZ plane for the spherical phantom sample containing a mixture of Soltrol and hexafluorobenzene. The glass bulb containing the fluid mixture had an internal diameter of 3.2 mm; the images contain 128 x 128 pixels each. Figure 3–13*A* shows the proton image obtained at a frequency of 270.1 MHz. Figure 3–13*B* shows the 19F image obtained at a frequency of 254.0 MHz using the same magnetic field imaging gradients as for the proton image. Figure 3–13*C* shows the same image data set used in 3–13*B*, but scaled by the ratio of 270.1/254.0. Comparison of the images in Figure 3–13*A* and 3–13*C* indicates they are identical in size and shape. Comparisons of multinuclear images for two-phase rock/fluid images can now be made in confidence.

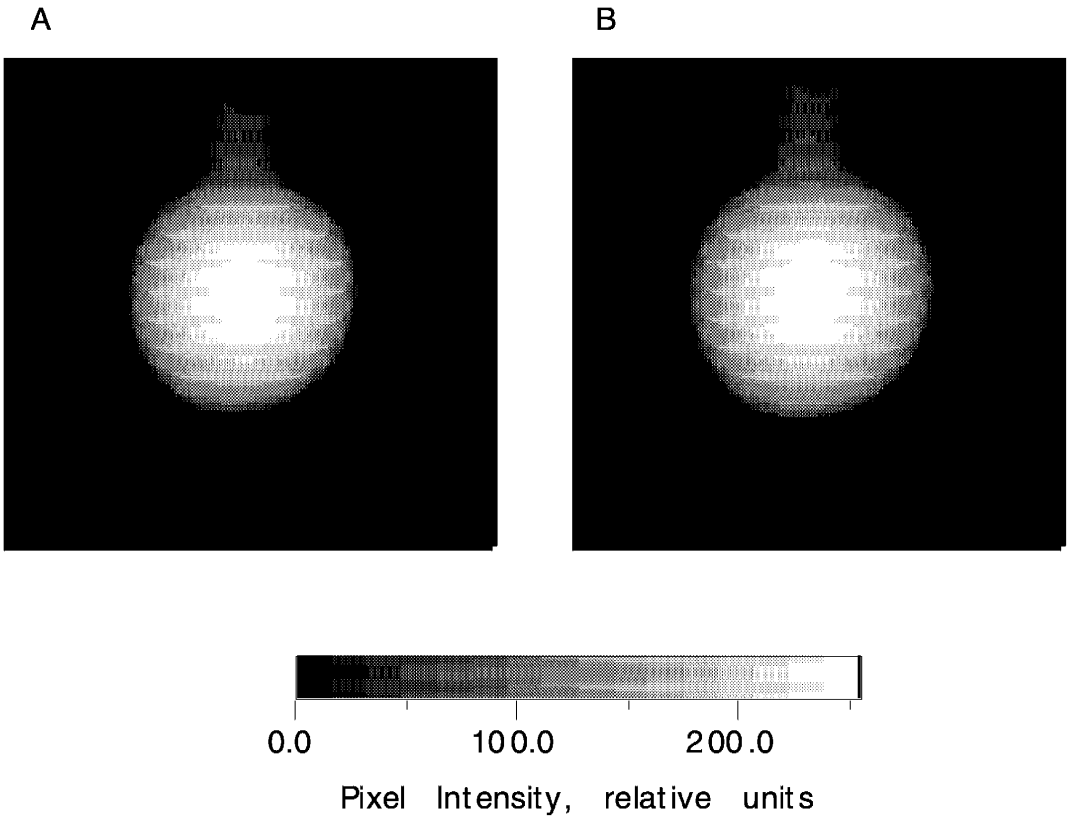

Figure 3–12 Multinuclear MR Images of the Fluid-Filled Spherical Glass Bulb. *A*, imaged using 19F NMR; *B*, imaged using proton NMR. The proton image is slightly larger because the size of the image in a given magnetic gradient scales with the respective NMR frequencies of detection.

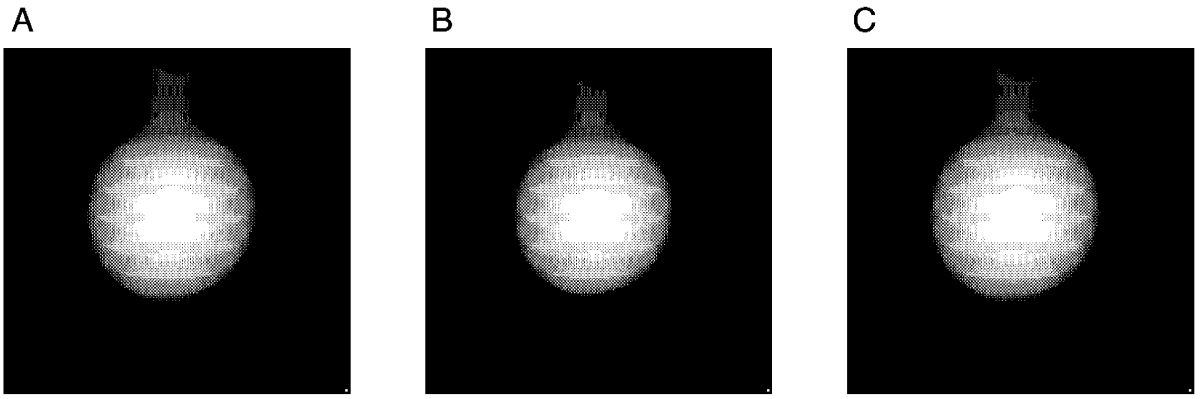

Figure 3–13 Multinuclear MR Images of the Fluid-Filled Spherical Glass Bulb. *A*, imaged using proton MR; *B*, imaged using 19F MR; *C*, scaled 19F image. The proton image is slightly larger because the size of the image in a given magnetic gradient scales with the respective MR frequencies of detection.

3.8 Oil/Brine Saturation Measurements In Sandstone

Multinuclear MRI experiments were run on a two-phase fluid system using a small Bentheim sandstone core plug (5.4 mm diameter x 7.2 mm long). The core plug was mounted in the Teflon core holder as previously described and saturated under vacuum with 0.5% NaCl containing 0.023% MnCl2 as relaxation agent. The hydrocarbon phase was hexafluorobenzene to permit imaging the oil phase at 19F frequency. The following series of imaging experiments were run at both proton and 19F frequencies:

- The brine-saturated core plug (proton)
- Residual brine after flowing 10 PV oil (proton)
- Residual oil after flowing 10 PV brine (proton and 19F)
- Residual oil after 50 PV brine (19F and proton)

The same imaging gradient strengths were used for both the proton and 19F images. Both 2D and 3D images were acquired at each stage. Figure 3–14 shows XZ views of the 2D images, with the 19F images scaled as described previously. The direction of fluid flow was from bottom to top in all the views. Figure 3–14*A* shows the initial brine-saturated core plug, while the residual brine phase is shown in Figure 314*B*. Subtracting image B from A gives the oil saturation at residual brine shown in Figure 3–14*C*. Figure 3–14*D* shows the brine phase (after 10 PV) at residual oil while Figure 3–14*E* shows the residual oil. Adding images *D* and *E* gives the total fluid at residual oil, shown in Figure 3–14F. Figure 3–14*G* shows the brine phase (after 50 PV) while Figure 3–14*H* shows the residual oil. Figure 3–14*I* shows an XY view of the brine-saturated core plug. It is clear from the above discussion the residual brine and oil data measured by 19*F* and subtraction gave the same results.

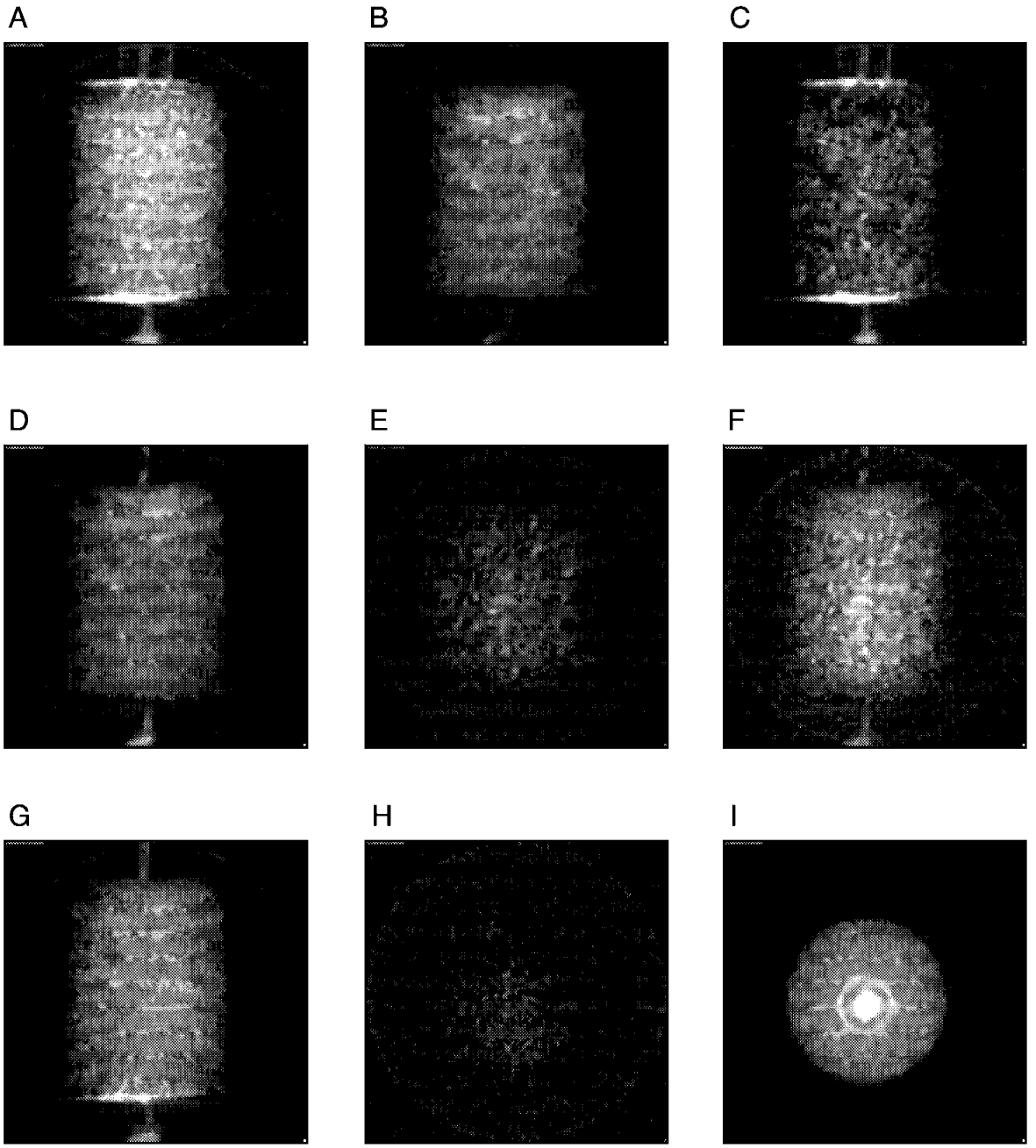

Figure 3–14 **Multinuclear MRI Images of a Brine/Hexafluorobenzene Saturated Bentheim Sandstone Core Plug. Shown are 2D images of the XZ views of the fluid-filled sandstone plug. *A*, Brine; *B*, residual brine (after 10 PV oil); *C*, oil at residual brine *(A-B)*; *D*, brine (after 10 PV) at residual oil; *E*, residual oil by 19F MRI; *F*, total fluid at residual oil *(D+E)*; *G*, brine (after 50 PV) at residual oil; *H*, residual oil by 19F MRI; *I*, an XY view of the brine-saturated core plug.**

3.9 Imaging Water Shutoff Experiments

To help understand the mechanism in water shutoff using certain polymers, sintered glass packs were prepared using of 20–38μ diameter beads. The beadpacks were prepared in glass tubing of 3.8 mm inside diameter. The ends of the beadpack (about 25 mm long) were fitted with end caps sealed on with O-rings. An Isotec pump was used to inject the various fluids into the beadpacks at controlled flow rates. Brine containing 1% NaCl with 0.023% MnCl2 was used as the aqueous phase and Soltrol 130 was used as the oil phase. Polyacrylamide polymer gel at 0.5% in the brine phase was used as the flow control agent. Five samples were run and imaged in the following sequence:

- Brine-saturated bead pack
- Soltrol 130 at residual brine saturation
- Brine at residual Soltrol 130 saturation
- Residual Soltrol 130 after polymer flood
- Soltrol 130 at residual brine saturation after polymer flood

Single slices from the 3D MRI of these five samples are shown in Figure 3–15. In these views, fluid injection was from right to left. Figure 3–15*C* had a much lower signal/noise ratio than the other experiments for some reason. More contrast was expected between the oil and brine phases in regions where polymer had blocked off-flow pathways. There are some hints of this in Figure 3–15*D* and 3–15*E*.

To unambiguously track the brine in two-phase measurements, the above experiments have been repeated using the same brine composition (1% NaCl with 0.023% $MnCl_2$) as the aqueous phase and a fluorinated compound 3,5-Bis (trifluoromethyl) bromobenzene as the oil phase. This compound has a sharp fluorine resonance peak and the three remaining aromatic protons provided negligible interference with proton imaging of the brine phase. Polyacrylamide polymer at 0.5% in the brine phase with the water replaced by deuterium oxide was used as the flow control agent. Five experiments were imaged:

- Brine-saturated beadpack
- Residual brine at oil saturation
- Brine at residual oil
- Brine at residual oil after polymer flood
- Residual brine at oil saturation after polymer flood

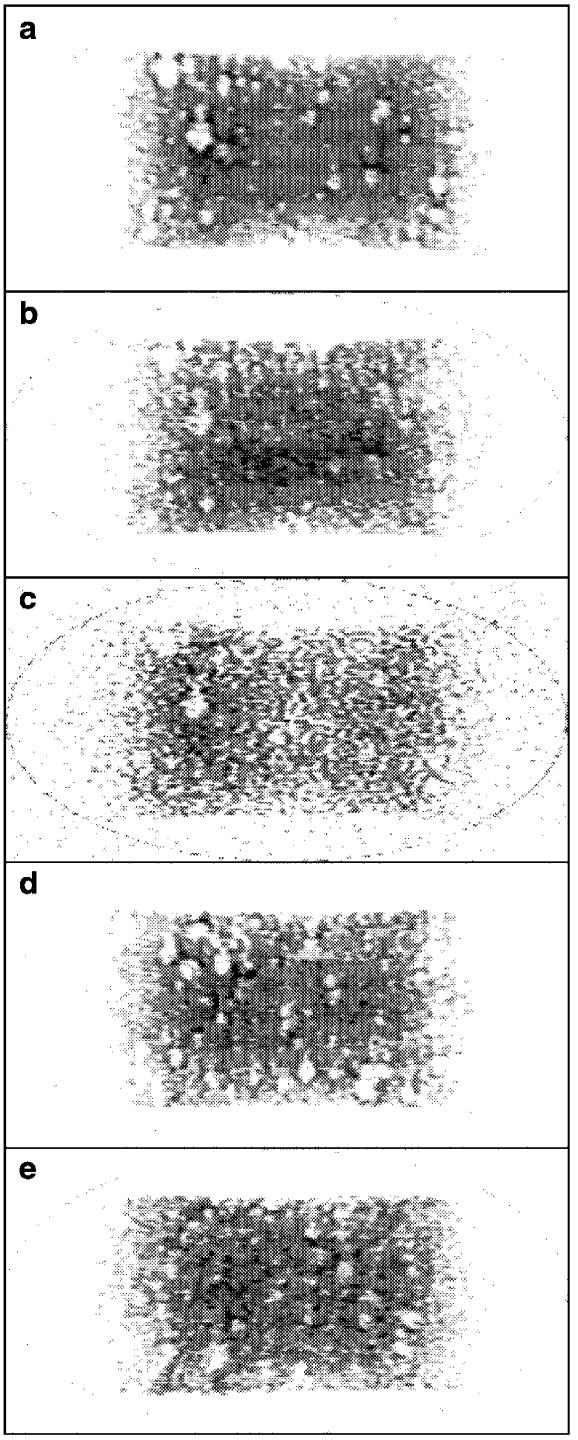

Figure 3–15 **MR Images of the Fluid-Filled Sintered Glass Beadpacks. *A*, Brine-saturated beadpack; *B*, Soltrol 130-saturated beadpack at residual brine; *C*, brine-saturated beadpack at residual oil; *D*, brine-saturated beadpack at residual oil after polymer flood; and *E*, Soltrol 130-saturated beadpack at residual brine after polymer flood.**

Single cross-sectional slices from the proton 3D MR images of these five experiments are shown in Figure 3–16. The images in the right-hand column of the figure (*C, E, G,* and *I*) show the respective oil phase obtained by subtracting the corresponding left-hand brine image from image 3–16*A*. The bright spot in each of the images in the right-hand column comes from the initial brine-saturated image (3–16*A*) through the subtraction process and does not necessarily represent a region of high fluid concentration. The dark spots in the images are areas where the beads completely fused together with little fluid saturation. Image 3–16*B* shows an irregular region where the residual brine concentration is somewhat higher. This same region is somewhat enhanced in image 3–16*H* after the polymer flood. For the most part, both fluids seem to be evenly distributed across the images with little evidence of regions within the beadpack where polymer had blocked off flow pathways. Fluorine imaging was used to image the beadpack after the last experiment, where the oil phase would be equivalent to Figure 3–16*I*. The signal/noise ratio was low and the image was of poor quality because the oil saturation was low and fluorine imaging sensitivity for the oil phase was about 25 % of that of proton imaging.

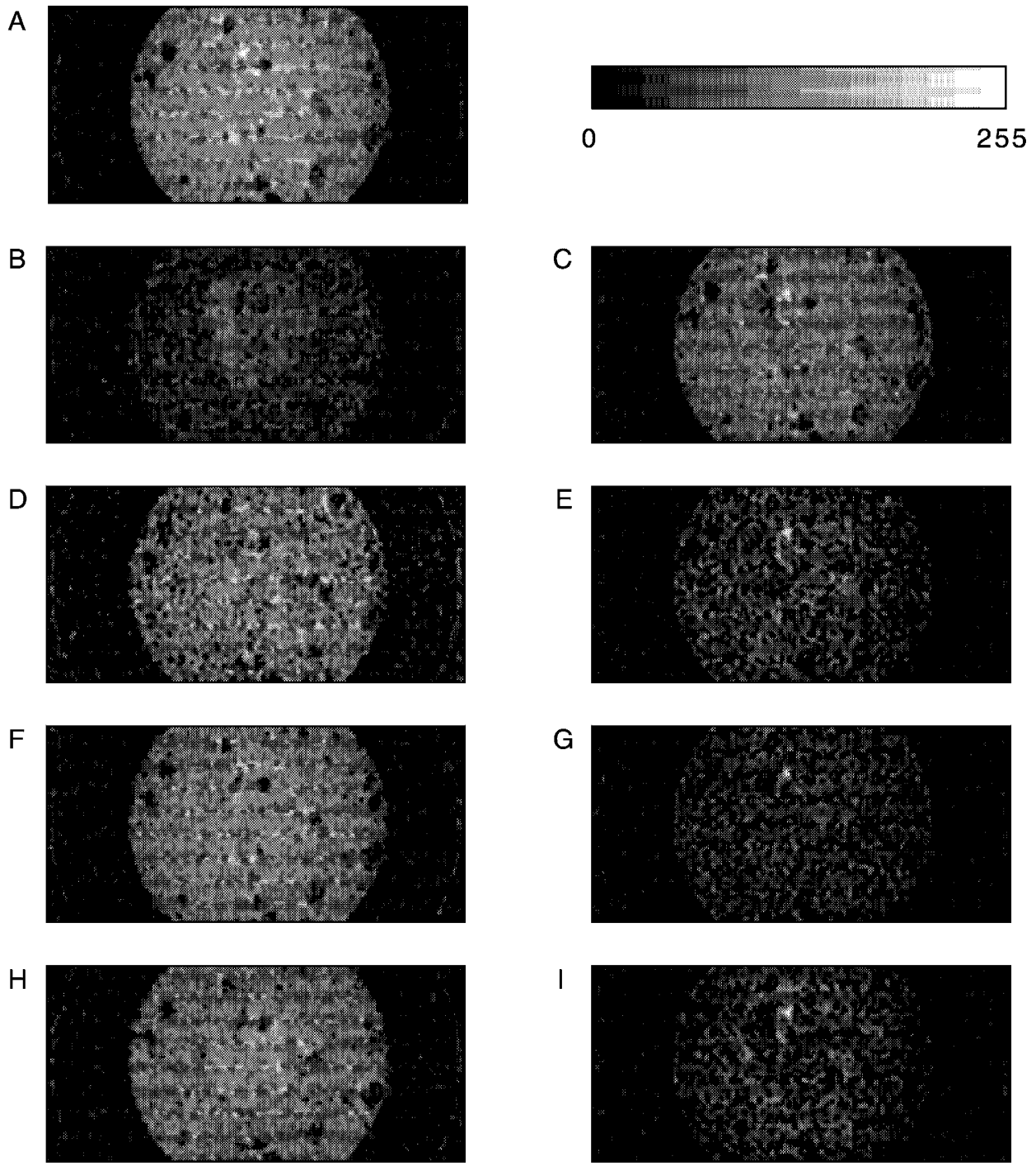

Figure 3–16 MR Images of the Fluid-Filled Sintered Glass Beadpack. *A*, Brine saturated beadpack; *B*, Residual brine; *C*, Oil at residual brine *(A-B)*; *D*, Brine at residual oil; *E*, Residual oil *(A-D)*; *F*, Brine at residual oil after polymer flood; *G*, Residual oil after polymer flood *(A-F)*; *H*, Residual brine after polymer flood; *I*, Oil at residual brine after polymer flood *(A-H)*.

3.10 Three-Dimensional Pore Connectivity in Two-Phase Systems

Figure 3–17 shows 2D MR images of four fluid-saturated pore systems: System A was an oil-saturated polymer beadpack with bead diameters from 125 to 250μ. A beadpack of identical size beads has a theoretical porosity of 42%. System B was a core plug of Fontainebleau sandstone of 12% porosity saturated with 0.5% NaCl brine containing 0.023% MnCl2. System *C* was a core plug of Bentheim sandstone of 24% porosity saturated with similar brine. System *D* was a second core plug of Bentheim sandstone from the same block also saturated with a similar brine. The fluid-filled pores within the samples are the lighter areas in the figures with the beads or rock grains being the dark areas. The intensity scale is an 8-bit grayscale showing 256 levels of arbitrary image intensity. The images show a considerable variation in appearance. The beadpack shows much more uniformity in image intensity and more uniformity in apparent pore size. The Fontainebleau image shows much greater variation in pixel intensity and pore size with isolated large pores separated by low porosity areas of much smaller pores. The two Bentheim images are similar and visually intermediate between the other two systems.

A 3D block 64 pixels on each edge was extracted from the center of each MRI data set for the four systems and binarized to a black-and-white image, where pixels at or above a selected intensity level were white and those below the reference intensity were black. The reference intensities were selected to reflect the nominal porosities of the four systems. Image analysis software, developed at NIPER, can take the binarized 3D data set and track the porosity through the 3D image space and develop a histogram of pore size. This software also can perform up to six successive erosions and dilations on the binarized image before producing a histogram of pore size. This approach of using increasing stages of erosion/dilation to characterize rock images was developed originally for application to 2D petrographic images from thin sections (Ehrlich, 1984). Figure 3–18 shows results of this image analysis on the four systems. In Image 3–18*A*, the largest pore in the histogram expressed as a fraction of the total porosity remaining at each stage is plotted vs. the number of successive erosion/dilation stages. In the beadpack even after one stage of erosion/dilation, essentially all the porosity is contained in one large pore throughout the image pore space. The largest pore size then falls off after additional erosion/dilations. In contrast to the beadpack, the results for the Fontainebleau system show an opposite trend. The largest pore size starts off small and then increases modestly after several erosion/dilation stages. The Bentheim systems show an intermediate character with the earlier stages similar to the beadpack, but after two stages of erosion/dilation behaving similarly to the Fontainebleau system.

Image 3–18*B* plots the number of separate pores counted at each stage vs. the number of erosion/dilations for the four systems. The pores appear separated—not because they are unconnected, but because the size of the pore throats is below the detectable resolution of the MRI process. In Image *B*, for the beadpack, the number of pores starts off at one then increases modestly after two or three erosion/dilation and stages. For the Fontainebleau system, the number of pores is high with no erosion/dilations and then falls off almost exponentially with successive stages of erosion/dilation. The Bentheim systems again are intermediate in behavior with modest increase in the number of pores after one stage of erosion/dilation and then a decrease in the number of pores after additional erosion/dilations. The behavior of the four pore systems may be explained by considering the network of pores in the system. The beadpack with its homogeneous grain size and uncemented structure has an open pore network with no restrictive pore throats. Thus, the porosity occupies one large pore space of high connectivity. Several stages of erosion/dilation are required to break the connectivity and increase the number of separate pores. In contrast to this open system, the Fontainebleau system has isolated larger pores and many smaller pores connected by relatively narrow pore throats that are below the resolution of the MR image. Each stage of erosion/dilation eliminates more of the numerous small pores without greatly increasing the fractional size occupied by the largest pores. The Bentheim systems apparently have a generally homogenous pore system that is well connected and behaves similarly to the beadpack initially. However, the pore throats are smaller than in the beadpack, and so one stage of erosion/dilation starts to break the connectivity. After a few stages, the system is more like the Fontainebleau.

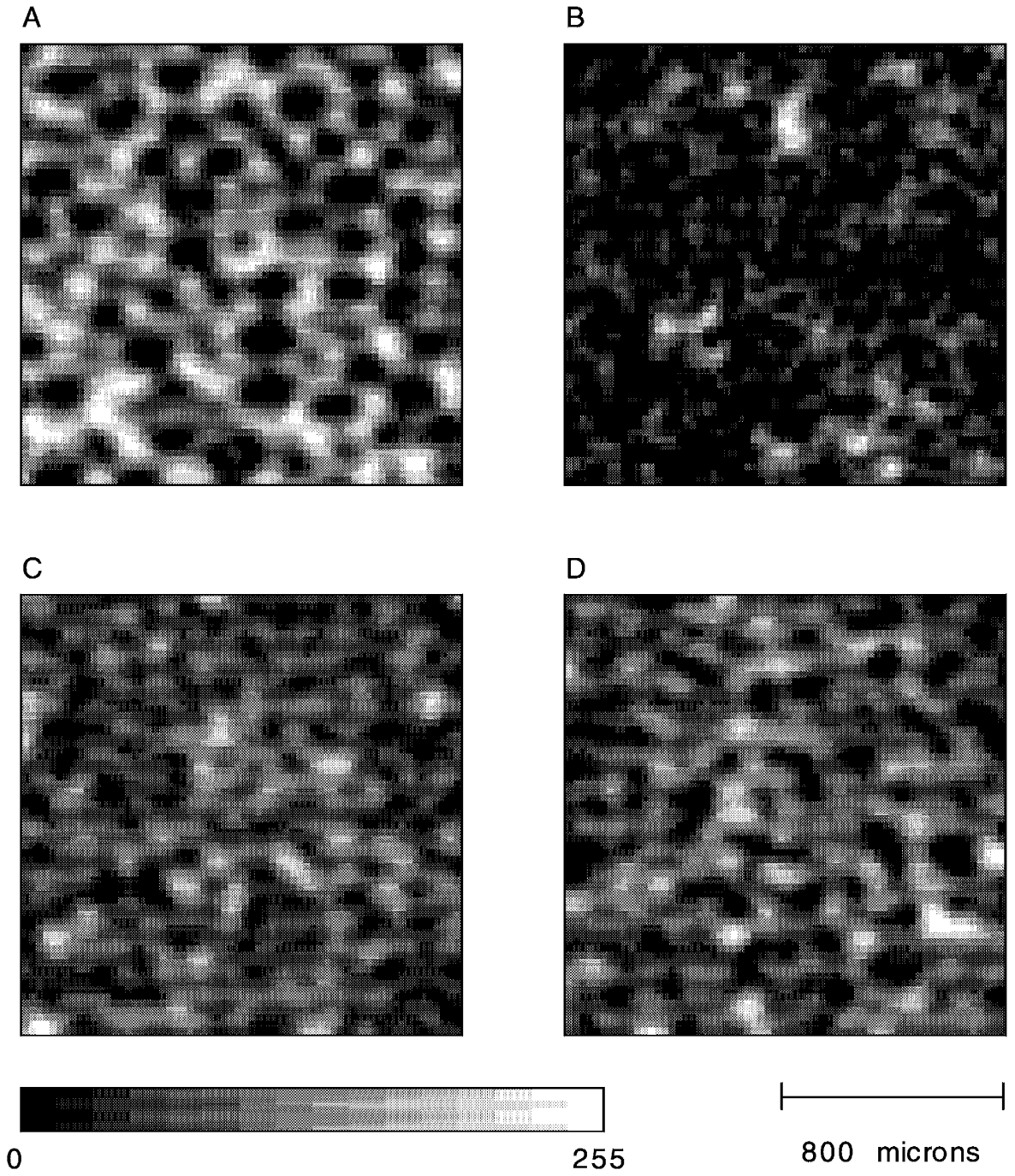

Figure 3–17 **Two-Dimensional MR Images of Fluid Saturated Pore Systems. *A*, Polymer beadpack (125-250μ); *B*, Fontainebleau sandstone, *C*, Bentheim sandstone; *D*, Bentheim sandstone #2. The lighter areas are the fluid-filled pores and the dark areas are the beads or rock grains. All images are at approximately the same scale.**

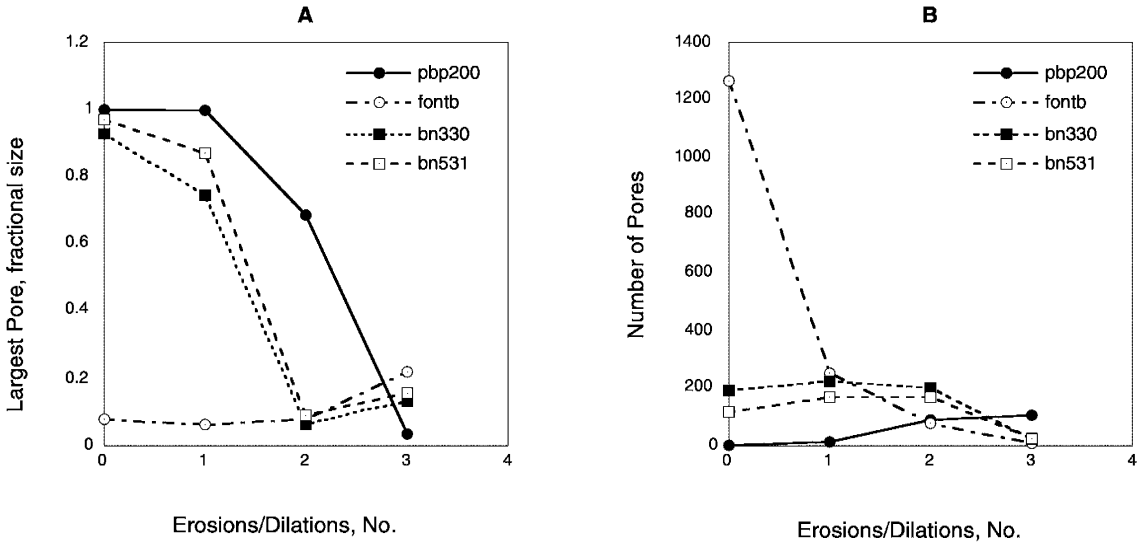

Figure 3–18 **Erosion/Dilation Image Analysis of Binarized MR Images. *A*, Fractional size of largest pore plotted vs. number of stages of erosion/dilation; *B*, Apparent number of separate pores plotted vs. number of erosion/dilation stages. (pbp200 = beadpack, fontb = Fontainebleau, bn330 = Bentheim #1, bn531 = Bentheim #2)**

4.0 SUMMARY

A technique of MR microscopy has been developed at NIPER using the projection reconstruction pulse sequence on small core plugs with strong imaging gradients. This method has successfully imaged fluids at pore scale in typical sandstones. Resolutions as high as 25 μm have been achieved.

A core holder has been developed constructed entirely from Teflon rod and two types of Teflon shrink tubing. It contains no protons to interfere with proton MRI signals from sample fluids. The core holder permits the fluids in the core plug to be exchanged without removing the sample from the imaging probe, allowing multiple fluid saturation images to be compared.

The technique has been modified to permit multinuclear imaging of two-phase fluid systems 59 59where the oil phase has the protons replaced by Fluorine-19. Unambiguous images of the separate water and oil phases can be obtained.

Software has been developed at NIPER which can perform a true 3D erosion/dilation process on the binarized data from a 3D MR image. Companion software can then perform a pore size measurement on the binarized data and track the pore connectivity through three dimensions. Early results show significant differences in the nature of the pore network in Fontainebleau and Bentheim sandstones.

5.0 REFERENCES

Doughty, Daryl A., Liviu Tomutsa, and Michael P. Madden. 1993. Pore Scale Fluid Imaging in Reservoir Rock by NMR Microscopy, ACS National Spring Meeting Symposium on Applications of Magnetic Resonance Imaging in Enhanced Oil Recovery, March 28 - April 2, Denver, Colorado.

Tomutsa, Liviu, Daryl A. Doughty, and Alan Brinkmeyer. 1992. Integration of Computed Tomography, Nuclear Magnetic Resonance Microscopy, Computer Assisted Petrographic Image Analysis and Flow Simulation for Heterogeneous Core Characterization. Society of Petroleum Engineers Forum Series in North America, Frontiers in Technology, Special Core Analysis and Applications to Reservoir Engineering, July 12-17, Snowmass Village, Colorado.

Doughty, Daryl A. and Liviu Tomutsa. 1992. NMR Microscopy for Fluid Imaging at Pore Scale in Reservoir Rock. Joint Society of Core Analysts/Society of Professional Well Log Analysts Symposium, June 14-17, Oklahoma City, Oklahoma.

Robinson, M. A. and H. A. Deans. 1991. MRI Measurement of Oil Core Porosity Distributions. 32nd Experimental Nuclear Magnetic Resonance Conference, April 7-11, St. Louis, Missouri.

Mahmood, Syed M., Daryl A. Doughty, Liviu Tomutsa, and Matt Honapour. 1990. Pore Level Fluid Imaging Using High Resolution Nuclear Magnetic Resonance Imaging and Thin Slab Micromodels. Society of Core Analysts Fourth Annual Technical Conference, August 13-15, Dallas, Texas.

Doughty, Daryl A., and Nicida L. Maerefat. 1989. Preliminary Transformation of an NMR Spectrometer into an NMR Imager for Evaluating Fluid Content and Rock Properties of Core Samples. *The Log Analyst*, March-April: p. 78.

Doughty, Daryl A., and Nicida L. Maerefat. 1988. Modifications to a JEOL GX270 Wide bore Spectrometer for Magnetic Resonance Imaging: Petrographic Applications. Twenty-Ninth Experimental Nuclear Magnetic Resonance Spectroscopy Conference, April 17-21, Rochester, New York.

Doughty, Daryl A., and Nicida L. Maerefat. Transformation of an NMR Spectrometer into an NMR Imager for Evaluating Fluid Content and Rock Properties of Core Samples. Society of Core Analysts First Annual Technical Conference, Dallas, Texas, August 19-21, 1987.

Dumoulin, C. L. 1987. Nuclear Magnetic Resonance Imaging. *Spectroscopy*, v. 2, no. 1: p. 32.

Ehrlich, R., S. J. Crabtree, S. K. Kennedy, and R. L. Cannon. 1984. Petrographic Image Analysis I, Analysis of Reservoir Pore Complexes. *Journal of Sedimentary Petrology*, v. 54: pp. 1365-1376.

Huesman, R. H., G. T. Gullberg, W. L. Greenberg, and T. F. Budinger. 1977. *RECLBL Library Users Manual: Donner Algorithms for Reconstruction Tomography.* Berkeley, California: Lawrence Berkeley Laboratory, University of California.

APPENDIX

A.1 Ripple-Bedded Sandstone Upscaling

A.1.1 Introduction

The objectives of the rock-fluid imaging project are: (1) to develop a methodology to derive reservoir engineering parameters from petrographics, X-ray computed tomography (CT) scanning, and MR images, and (2) to investigate the applicability of imaging technologies to the development of scaleup procedures from core plug to whole core.

This year's effort is part of a multiyear plan to investigate methods of integration of multiscale rock and fluid properties of heterogeneous systems (ripple, crossbedded, and layered) for improved determination of reservoir properties to be used in reservoir simulation. This includes the use of simulation, CT (systems) and NMR (high-field multinuclear imaging of two- and three-phase fluid systems and low-field proton imaging) and logging data.

A sample has been selected in the previous fiscal year from a ripple-bedded facies present in the Bartlesville sandstone. The sample outcrop location has been described in a previous report (NIPER/BDM-0068). This sample represents a facies from which, due to its high permeability contrasts and small scale compartmentalization, oil recovery presents significant challenges. To predict the reservoir scale fluid behavior in such facies, information at various scales is necessary. In this work, the emphasis is on centimeter scale, which is comparable with the ripple dimensions. The rock heterogeneity is described in detail and flow studies are performed with the goal to identify the main rock fluid interactions that control the recovery of oil from this facies. Probe minipermeametry has been used to map the permeability heterogeneity on all six sides of the sample. X-ray CT was used to measure the porosity distribution and fluid saturations within the sample. Thin section petrographic image analysis has been used to determine the porosity permeability correlation at a scale comparable to the scale of the volume elements measured by the CT. Capillary pressures were measured by using centrifuge and CT and spontaneous imbibition. Relative permeability of plugs selected from the same facies were measured using steady-state methodology developed at NIPER in another task. The work was performed in compliance with the environmental, safety, and health (ES&H) requirements by DOE.

A.1.2 Project Description

A.1.2.1 Permeability Measurements

In the ripple-bedded sample studied, the flow across the low permeability ripples is expected to control the oil recovery. To perform accurate simulations of the fluid flow and oil recovery processes, accurate and detailed permeability values throughout the sample are needed. The permeability distribution on the surfaces defining the sample was previously determined by minipermeameter measurements. Measurements have been performed using the fully automated minipermeameter on a grid spacing of 5 mm along laminations and 2 mm across for a total of 33 rows x 33 columns for the largest surfaces of the sample. Good agreement was obtained between this series of measurements and the previous measurements on a 10 mm x 2 mm grid (Fig. A–1). The effect of the higher density grid is apparent in a better definition of the sedimentary structures in the sample.

The minipermeameter, which was constructed previously to perform automatic measurements along one axis, has been fully automated by adding a stepping motor and controller to the second axis and modifying the software for two-dimensional grid measurements. The software allows specification of arbitrary size rectangular grid patterns. For permeabilities in the 1–100 md range, a set of 1,000 measurements can be performed in less than 24 hours, with the equipment operating completely unattended. This compares to one week of operator time before automation. New software has been also written for rapid and accurate minipermeameter calibration using core plugs of known permeabilities as standards. The time for a calibration has been reduced to less than three hours. Calibration measurements and procedure testing were performed for the minipermeameter to ensure uniform accuracy (better than 3%) over the entire range of permeability (1–1,000 md). The calibrations showed very small equipment drift (flowmeters and pressure transducer). A scheduled calibration of these components at a six-month interval is recommended. To capture the permeability variations at the millimeter scale, the minipermeameter tip was modified to allow quick exchange of tip. Tips with inside diameter aperture as small as 0.9 mm have been built and used successfully.

A.1.2.2 Porosity Measurements

The Bartlesville sandstone (Bluejacket) block porosity has been measured by the standard procedure in which the sample is X-ray CT scanned both dry and saturated. A small container has been designed and built to reposition the sample in the scanner. Based on beam width and spacing between scans, the sample has been scanned in three modes: beam width 2 mm, spacing 2 mm (82 scans, highest resolution; beam width 4 mm, spacing 4 mm (41 scans, medium resolution; and beam width 4 mm, spacing 5 mm (33 scans, spacing matching minipermeameter measurement spacing). The minipermeameter measurements were performed on a 21 x 33 grid. The CT porosity measurements were performed initially on a 256 x 256 grid (the CT image dimensions) from which the actual rock image was cropped for a reduced grid of 100 x 165. To match the scales of the two measurements, the porosity of 25 pixels (5 x 5) was arithmetically averaged throughout the porosity image, generating an upscaled image with 20 x 33 grid blocks. The permeability and porosity images are displayed in Figure A–2. A good spatial correlation is

observed between the permeability (displayed on log scale) and porosity values. A curve fit for the permeability/porosity correlation obtained by plotting values from a single column of data from the center of the permeability/porosity data is shown in Figure A–3. Preliminary porosity measurements performed on the sample using whole-core magnetic resonance (MR) also show a spatial distribution consistent with the CT and minipermeameter data (see Fig. A–4). While the MR measurements can take considerably longer than the CT measurements (overnight vs. less than 30 minutes), they can provide information regarding porosity and pore size distribution. Further MR measurements are to be performed to investigate the relationship between the permeability and porosity and the pore size distribution.

A problem encountered in previous work with heterogeneous samples was the difficulty of achieving uniform oil saturations between inlet and outlet, due to the low flow rates (few feet/day) used during the oil flood. The low flow rates are caused by the low pressure gradient needed to prevent damage to the sample encapsulating material. Measurements on plugs showed the need for pressure differentials in hundreds of psi across the core to achieve a satisfactory oil initial saturation. Such pressures cannot be applied to the encapsulated sample without risking the fracturing of the epoxy. A procedure has been designed to allow increased fluid pressures by encapsulating the sample in a cylindrical (6-in. diameter) shape, placing the cylindrical sample in a sleeve in a large pressure vessel, and applying the overburden pressure to the encapsulated sample in the usual way. A new positioning system was designed and built to allow the replacement of the sample in the CT scanner in exactly the same position as before saturation. Testing of the positioning system shows an accuracy better than 0.4 mm (voxel size).

To understand the flow across the low permeability ripples, three-port end pieces have been designed which allow injection and production from various permeability layers and the study of the effect the ripples have on oil recovery. Each end piece has three rectangular ports matching major permeability layers in the sample (see Fig. A–5). The effect of end piece design on the fluid flow in the sample has been studied by performing both single- and two-phase simulations. The permeability distribution measured by the automated minipermeameter (see Fig. A–6) was used for input in the simulations. The simulations were performed for cases with the injections at either end of the sample, with fully open end pieces, with three-port end pieces and with crossflow (injection in top port and production at the lower port). Two cases were considered for vertical permeability: 1) vertical permeability equal to horizontal permeability, and 2) vertical permeability equal to one-tenth of the horizontal permeability (see Figs. A–7 through A–9). The simulations for both the open and three-port end pieces show similar flow patterns, with the simulations in which lower vertical permeability are used displaying stronger fingering. For both open and three-port end pieces, an early breakthrough takes place in the higher permeability layer located at the top of the sample. Even after approximately one pore volume injected, a significant part of the sample is left unswept. Eventually, after more than 1.5 pore volume injected, the sample is almost completely swept. The crossflow simulations, performed to test the effect of the three-port end piece design, showed the tracer first filling the high-perm layer and next moving across the low perm layer toward the open port. Simulations of oil floods using both the open and three-port end pieces were performed using dual relative permeability curves with a threshold of 7.25 md , which were based of measurements of relative permeability performed on plugs from the Glenpool field (Fig. A–10). Again, two cases were

considered for vertical permeability: 1) vertical permeability equal to horizontal permeability, and 2) vertical permeability equal to one-tenth of the horizontal permeability. As in the case of tracer simulations, the permeability contrasts cause a strong flow channeling. At approximately one pore volume oil injected (Figs. A–11 and A–12), a significant oil saturation gradient between inlet and outlet is observed. The above simulations show that using the three-port end pieces does not introduce extra channeling of the fluid flow in the heterogeneous sample. At the same time, the three-port configuration allows the study of crossflow and of flow channeling caused by the rock heterogeneity.

After completion of the simulation studies, the Bluejacket sample has been encapsulated. Nine pressure ports have been placed on each of the two large sides. These ports will allow pressure measurements that will be used to calculate the experimental effective permeability tensor for the Bartlesville sample. Comparison with theoretical values (numerical and analytical) will be made.

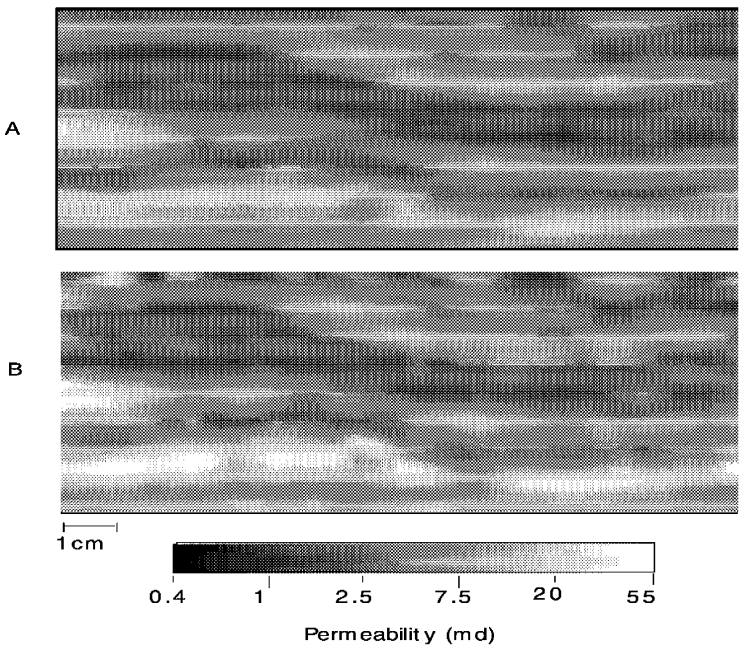

Figure A–1 Permeability Map of Bartlesville Sandstone Sample. Minipermeameter measurements are taken on a 10 mm x 2 mm grid *A*, and 5 mm x 2 mm grid *B*.

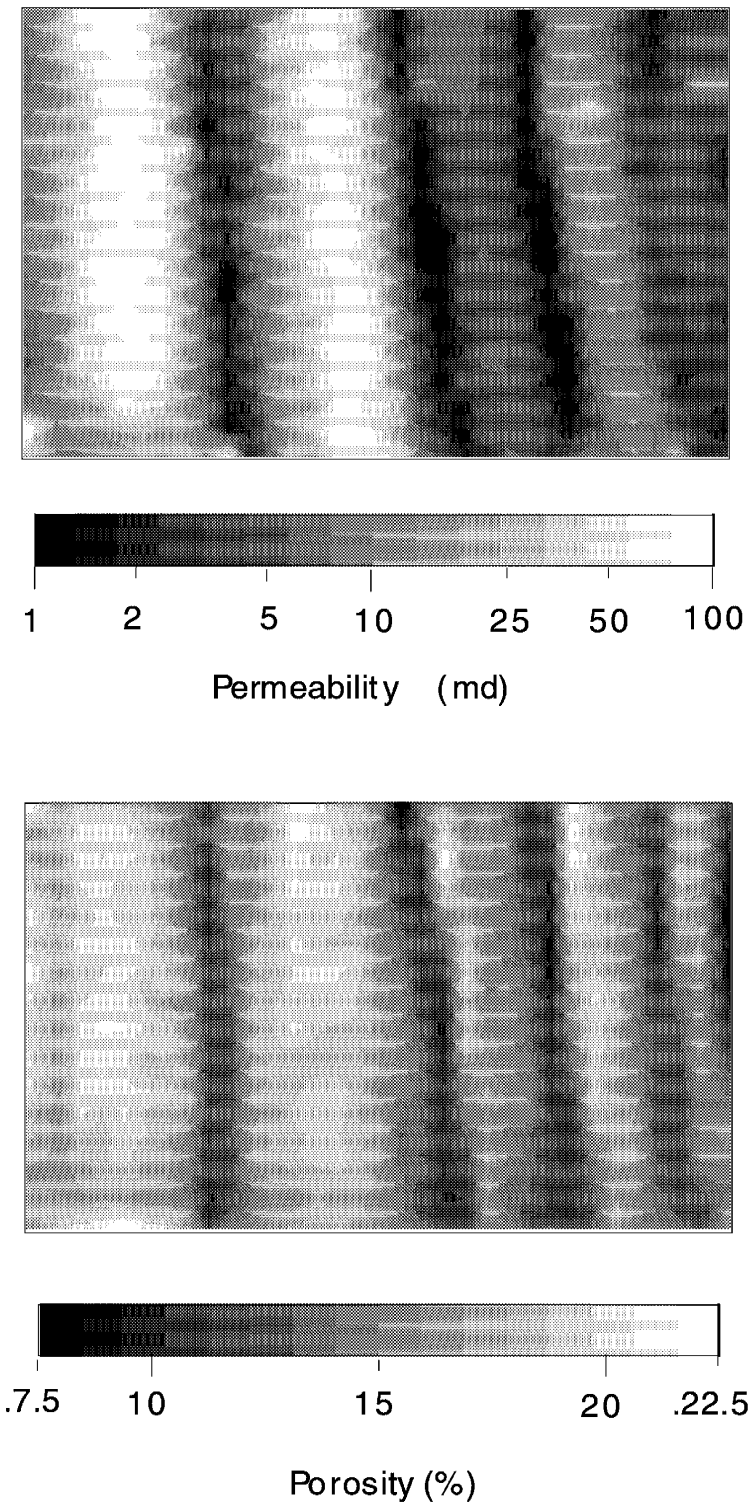

Figure A–2 **Comparison Between Minipermeameter Measured Permeability (top) and X-Ray CT Measured Porosity (bottom) for the Bluejacket Sandstone Sample.**

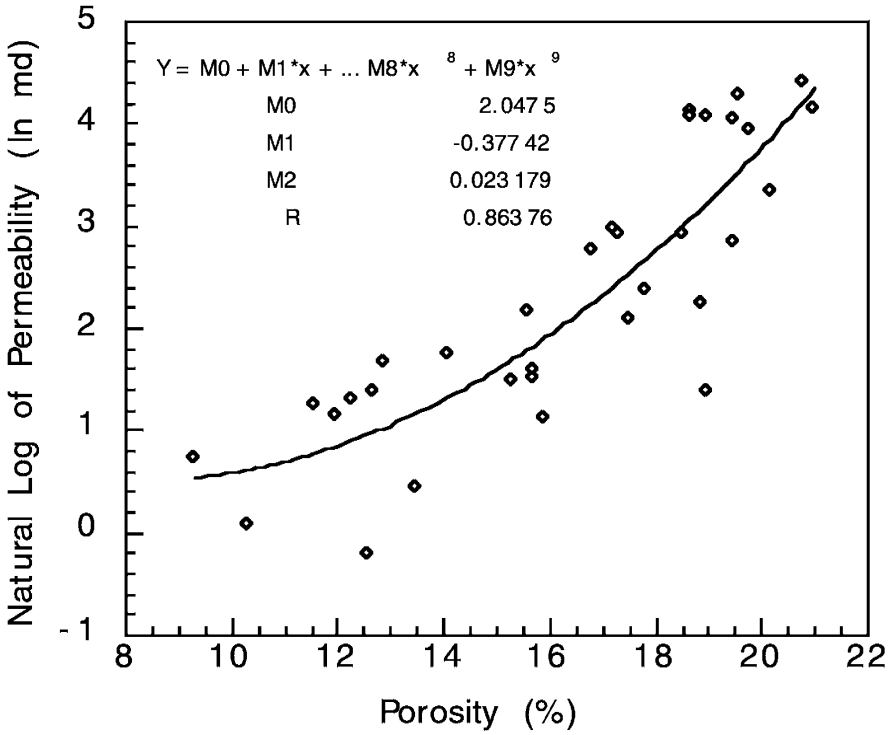

Figure A–3 **Permeability/Porosity Correlation Derived from Minipermeameter and CT Data.**

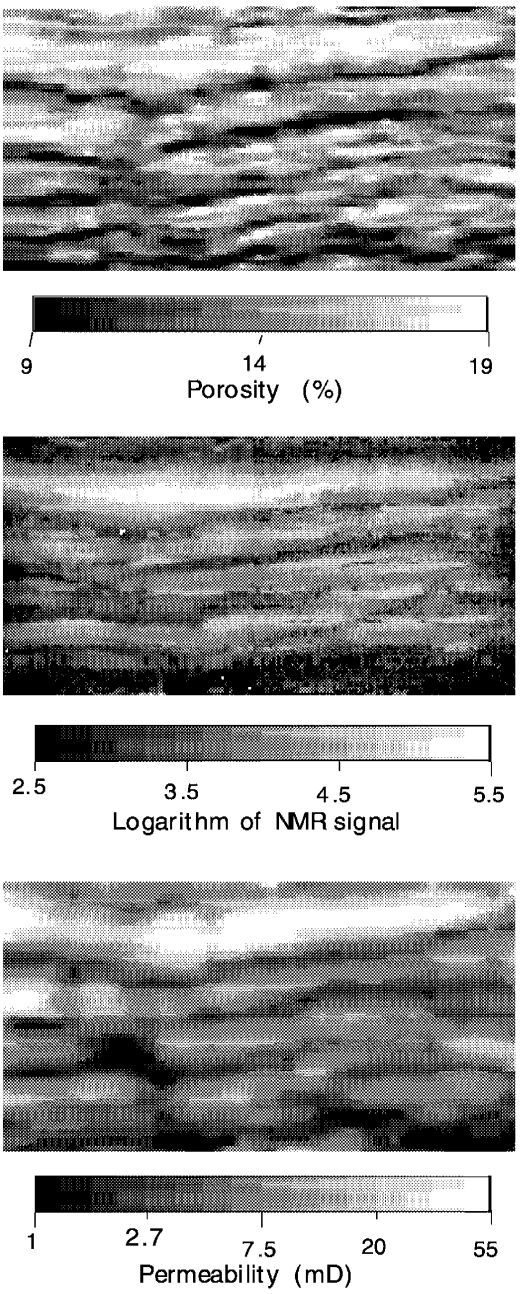

Figure A–4 **Comparison Between CT Porosity, MR Signal Strength, and Minipermeameter Permeability for Bartlesville Sandstone Sample.**

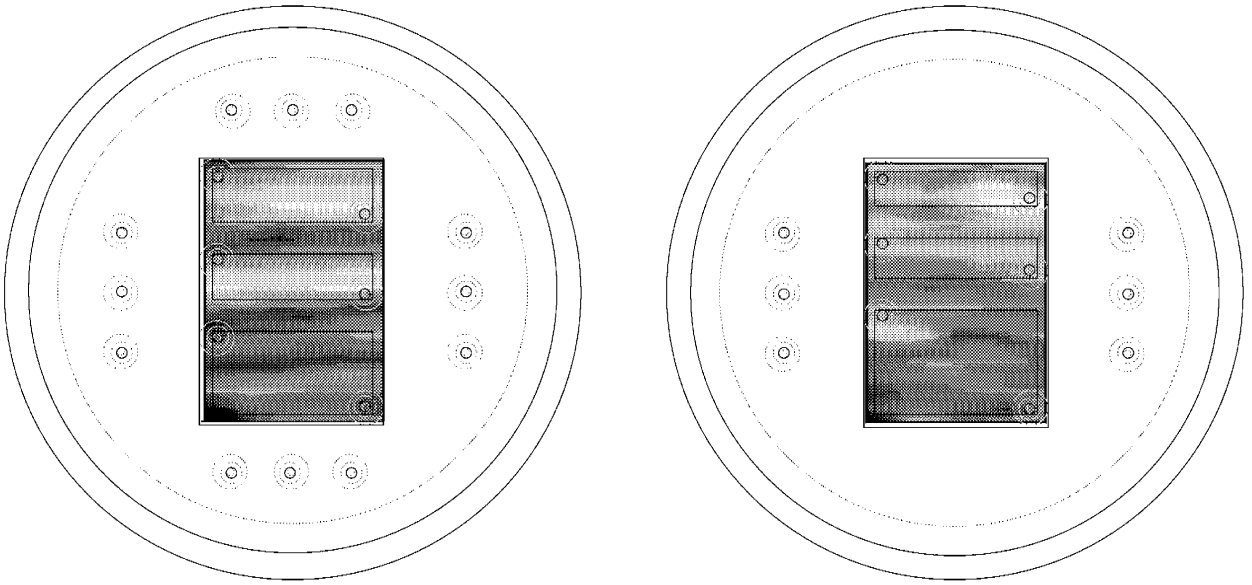

Figure A–5 **End Piece Design with Ports Matching Permeability Zones in the Bluejacket Sandstone Sample.**

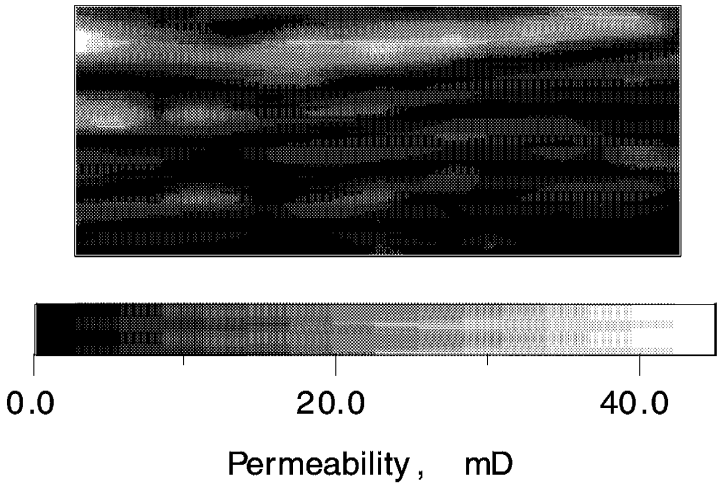

Figure A–6 **Permeability Distribution Used in Tracer and Oilflood Simulation in Bluejacket Sandstone.**

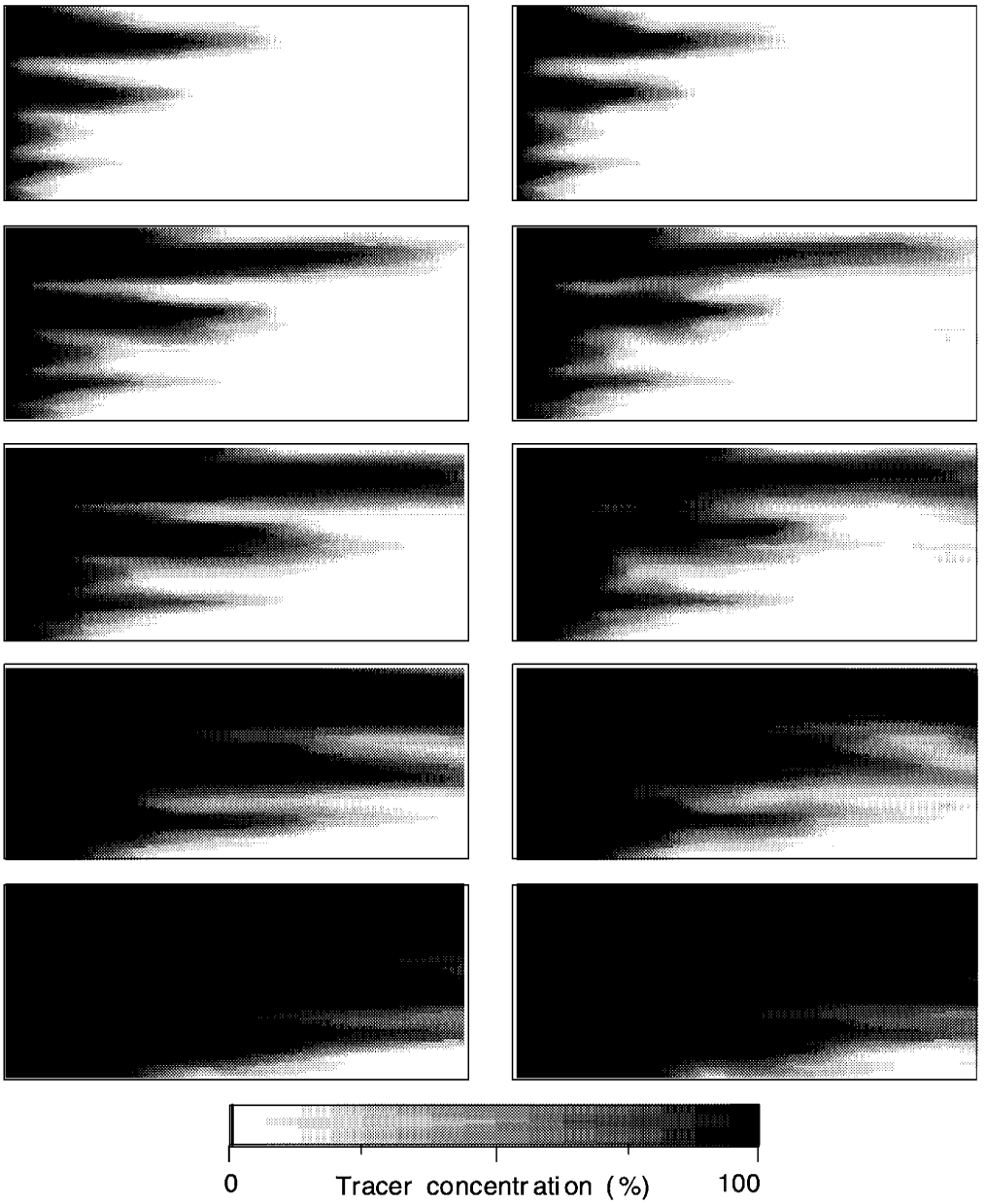

Figure A-7 **Simulations of Tracer Experiments in Bluejacket Sandstone. Injection was from left full face and production was at right open end piece. Vertical permeability (K_Z) in left views was 10% of horizontal (K_X). K_Z in right views was equal to K_X. Views after 0.19, 0.38, 0.57, 0.96, and 1.53 PV tracer injected.**

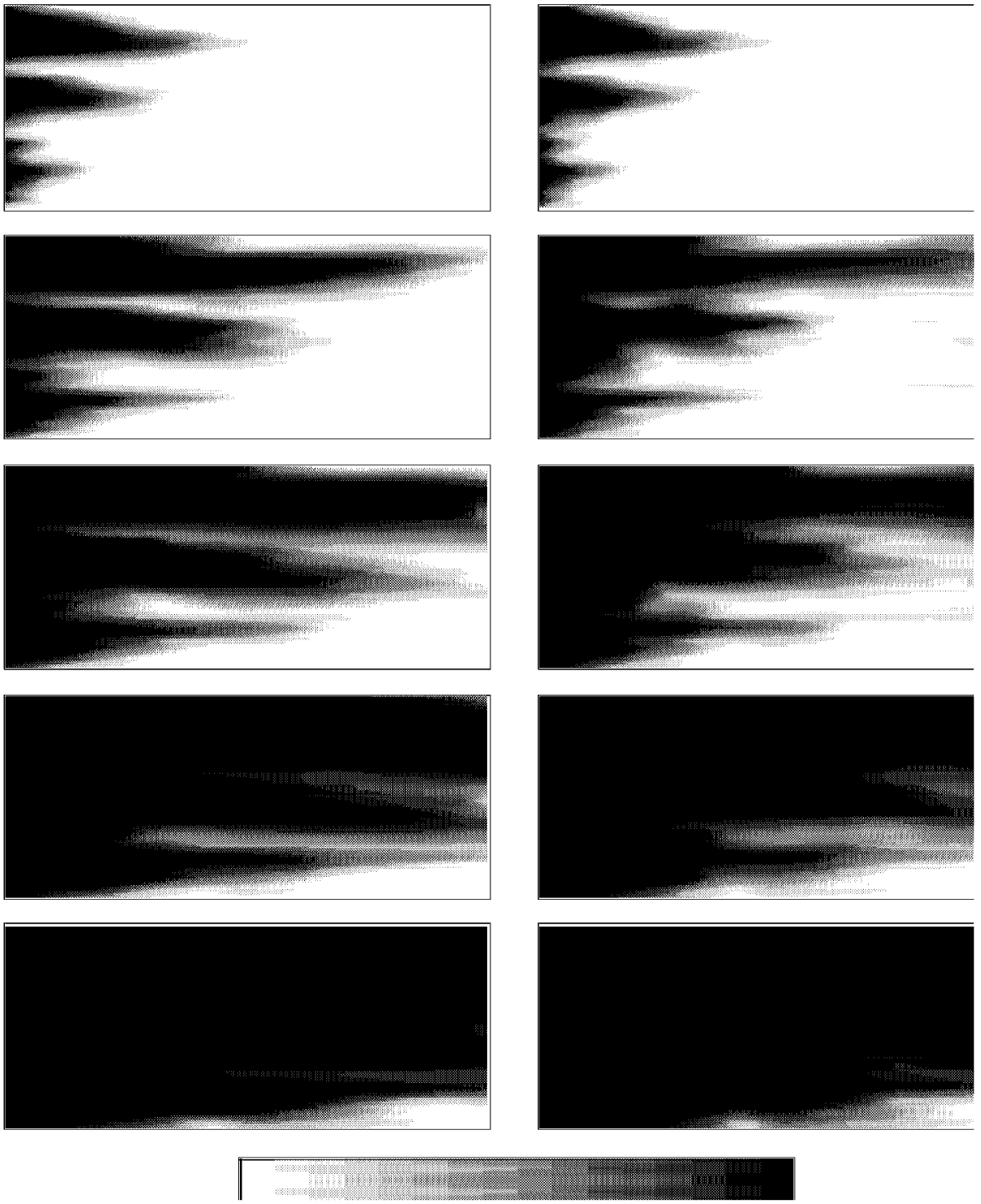

Figure A-8 **Simulations of Tracer Experiments in Bluejacket Sandstone. Injection was from left three-port face and production was at right three-port face. K_Z in left views was 10% of K_X. K_Z in right views was equal to K_X. Views after 0.14, 0.42, 0.69, 1.11, and 1.66 PV tracer injected.**

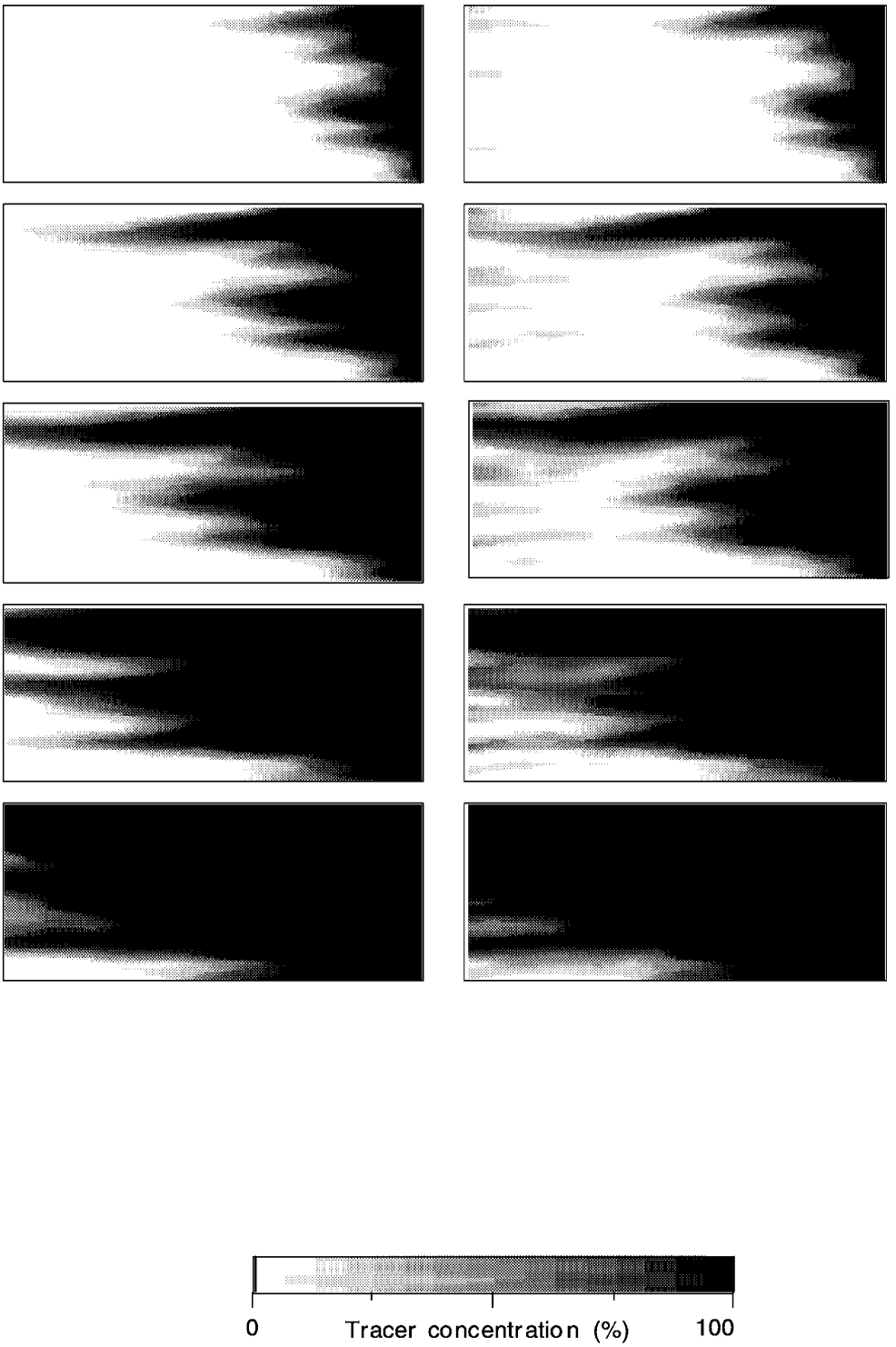

Figure A-9 **Simulations of Tracer Experiments in Bluejacket Sandstone. Injection was from right three-port face and production was at left three-port face. K_Z in left views was 10% of K_X. K_Z in right views was equal to K_X. Views after 0.14, 0.42, 0.69, 1.11, and 1.66 PV tracer injected.**

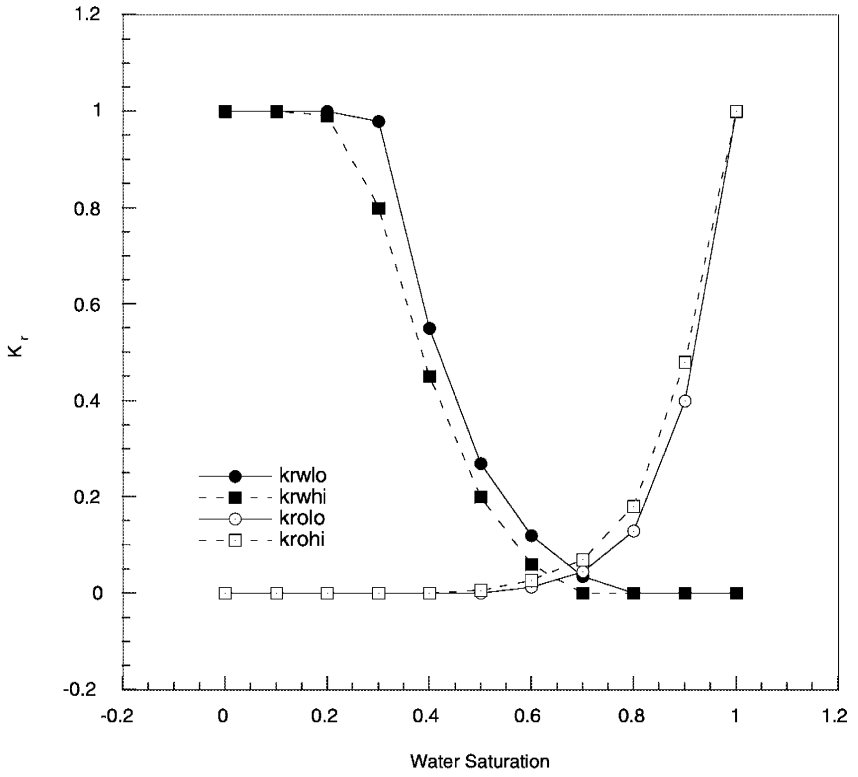

Figure A–10 Relative Permeability Curves used in Oilflood Simulations. The pairs of curves k_{rwlo}, k_{rwhi}, k_{rolo}, and k_{rohi} indicate curves for regions with permeability less than or higher than 7.25 md, respectively.

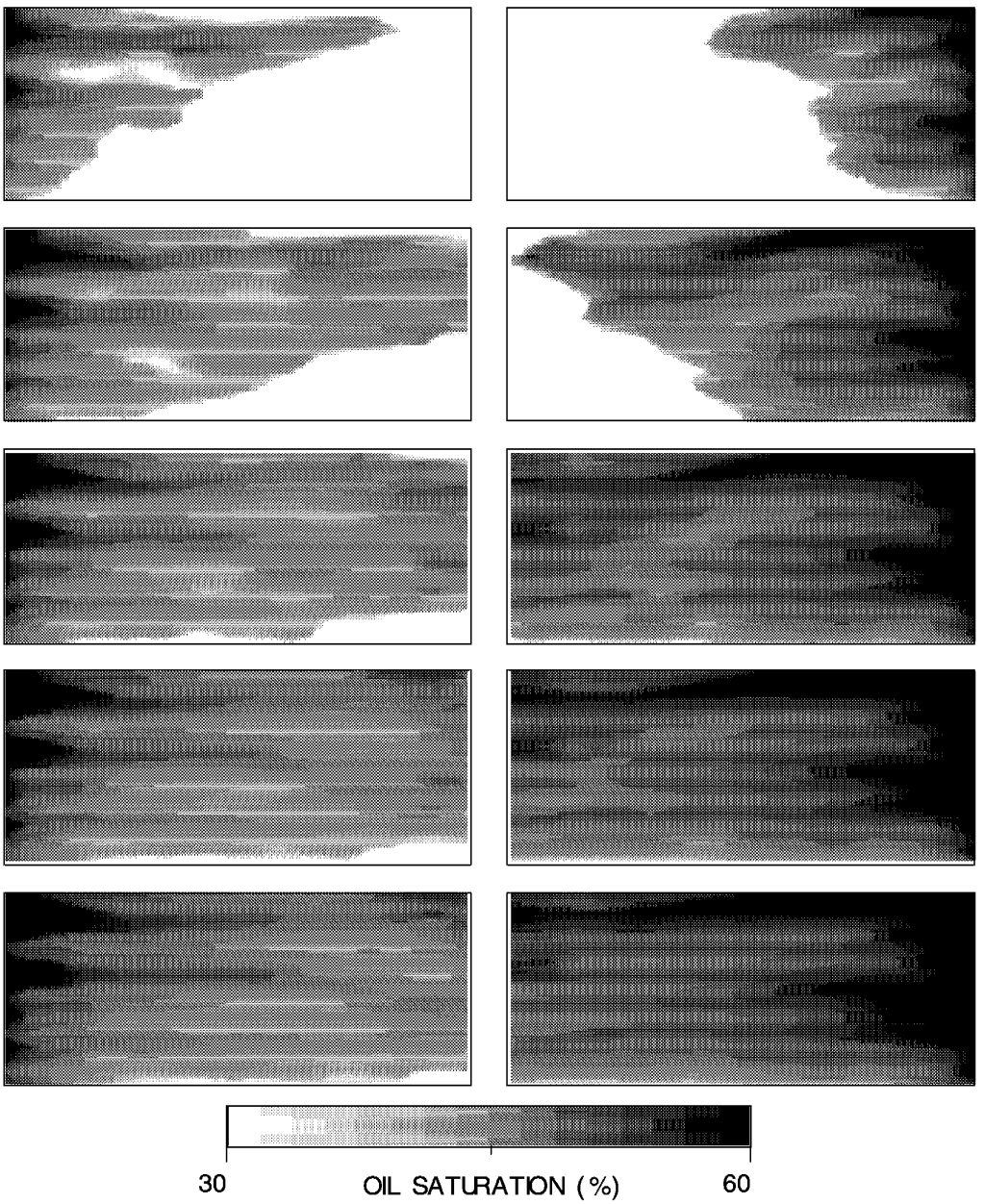

Figure A-11 **Oilflood Simulations in Bluejacket Sandstone Sample. Two sets of relative permeability data were used with the changeover occurring at 7.25 md. Injection in left views was from left full face and production was at right full-face end piece. Reverse flow injection/production was used in right views. K_z was equal to K_x. Views after 0.19, 0.38, 0.57, 0.77, and 0.96 PV oil injected.**

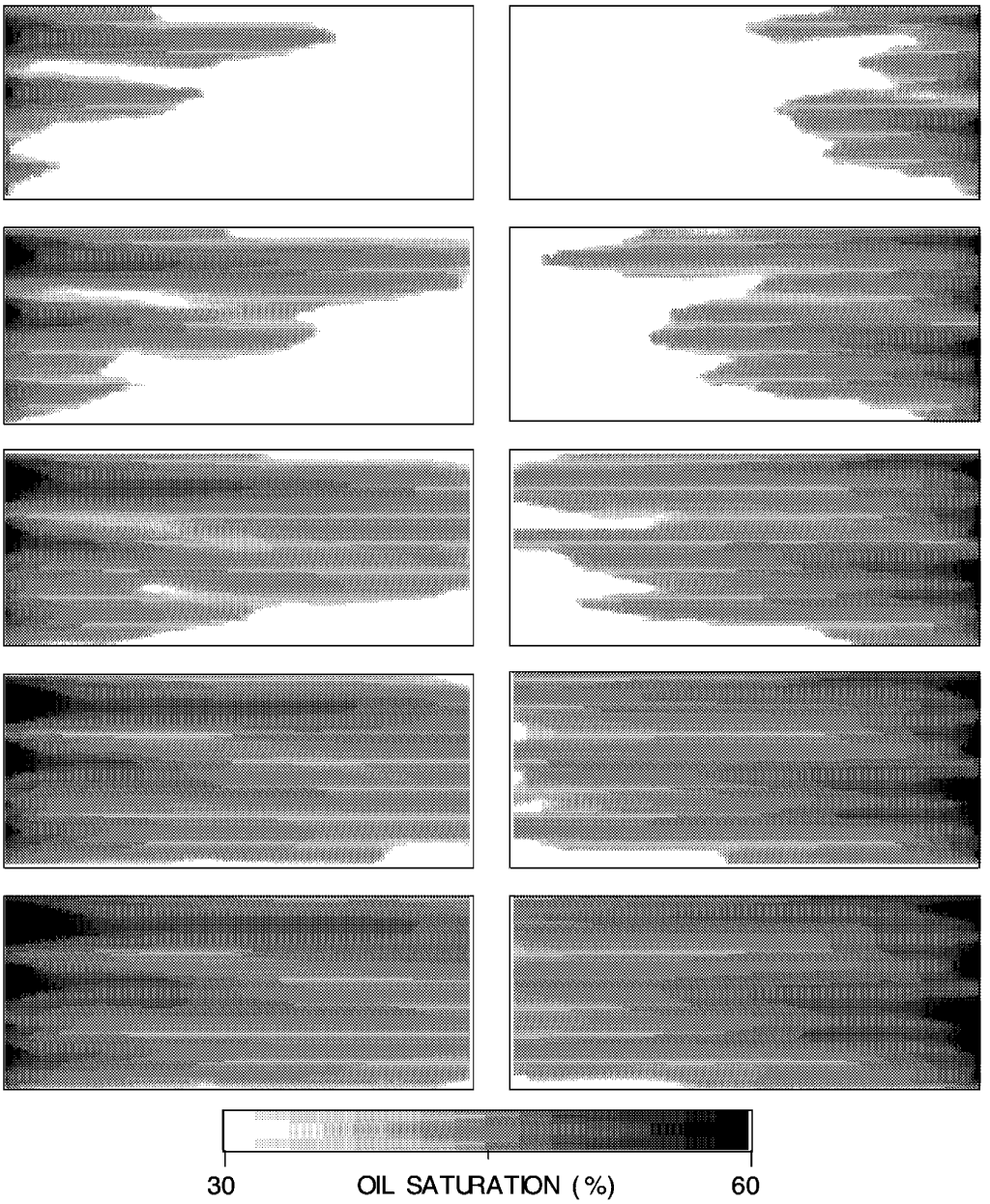

Figure A-12 **Oilflood Simulations in Bluejacket Sandstone Sample. Two sets of relative permeability data were used with the changeover occurring at 7.25 md. Injection in left views was from left three ports and production was at right three ports. Reverse-flow injection/production was used in right views. K_z was equal to 0.1 K_x. Views after 0.14, 0.28, 0.42, 0.69, and 0.98 PV oil injected.**

A.1.2.3 Petrographic Image Analysis (PIA)

The Petrographic Image analysis (PIA) method has been used for the calculating the porosity/permeability correlation needed for simulation of fluid movement in the sample. The location of the thin section and PIA-generated permeability map is shown in Figure A–13. Seven vertical profiles were taken at 4 mm spacing. Sixty measurements at 1 mm spacing were taken in each profile. The permeability/porosity correlation derived from PIA is shown in Figure A–14.

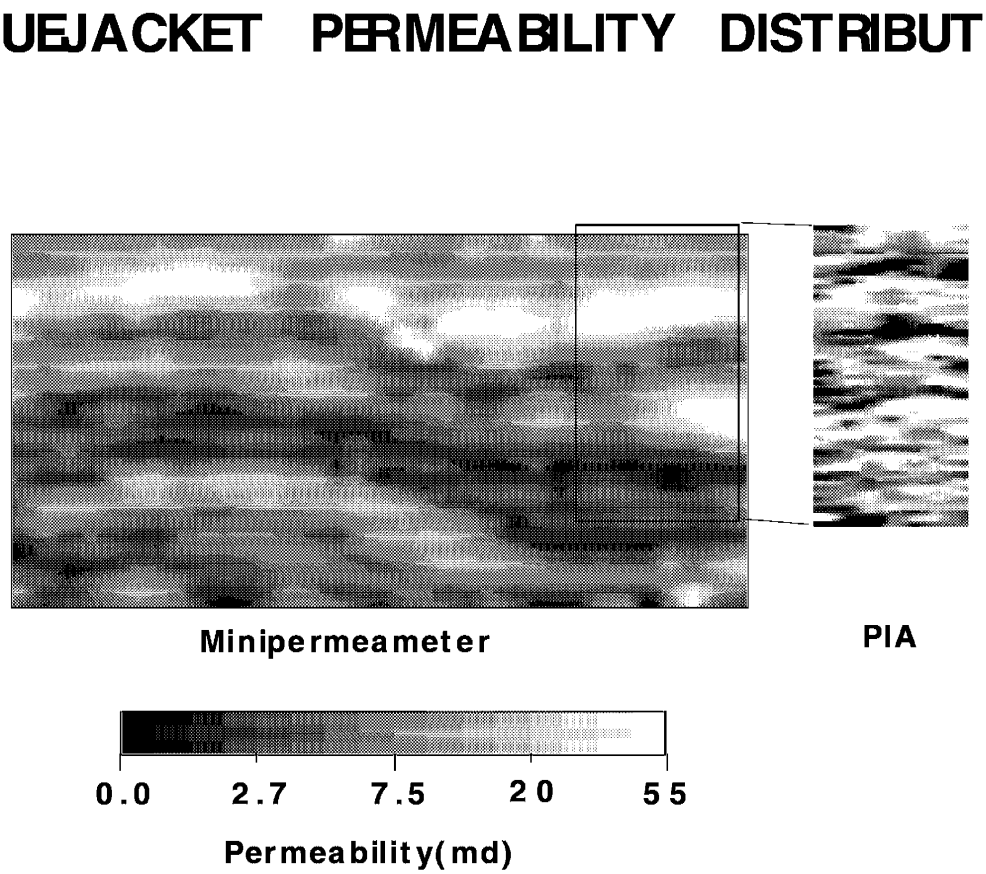

Figure A–13 Location of Thin Section (Black Border) and Permeability Map Generated by PIA

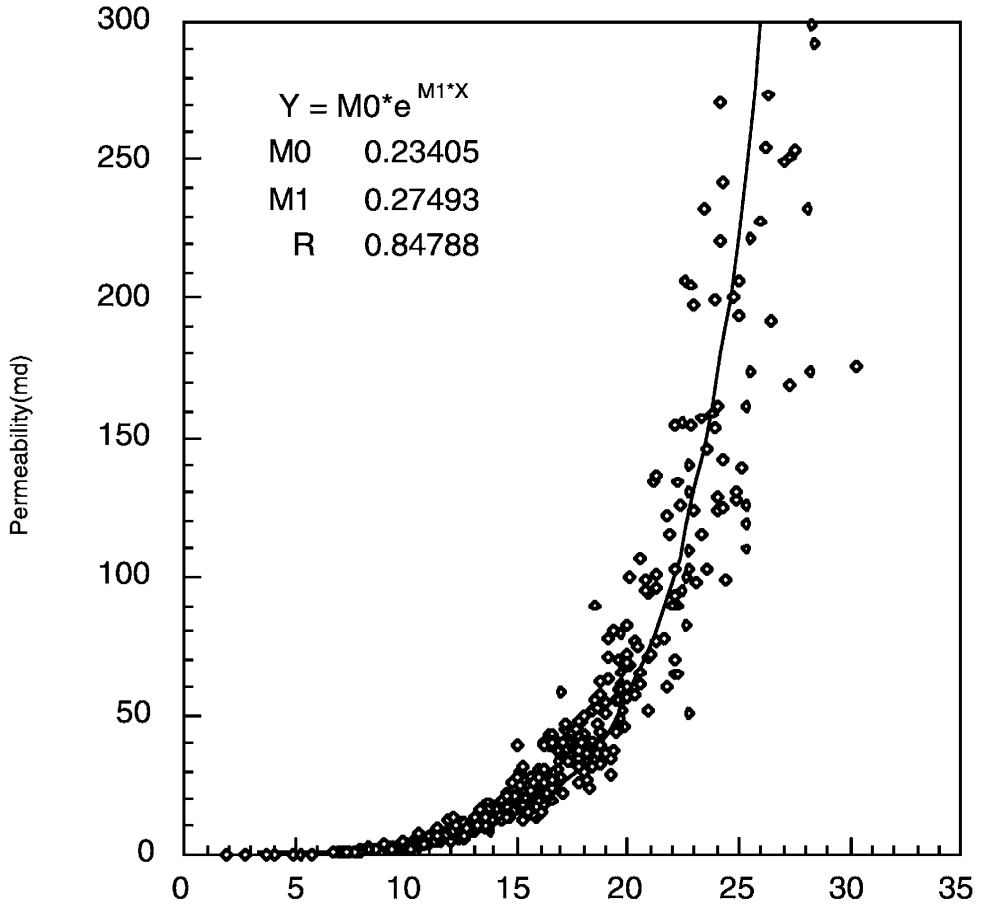

Figure A–14 Porosity/Permeability Correlation Generated by PIA

A.1.2.4 Relative Permeability

Relative permeability for two plugs cut parallel and perpendicular to the laminations were performed in Task 2. For plug scale measurements, three plugs were cut as shown in Figure A–15. Relative permeability for two plugs cut parallel and perpendicular to the laminations were performed in Task 2. The data will be used in simulating two-phase flow in the Bluejacket slab and upscaling the relative permeability data from plug to block scale.

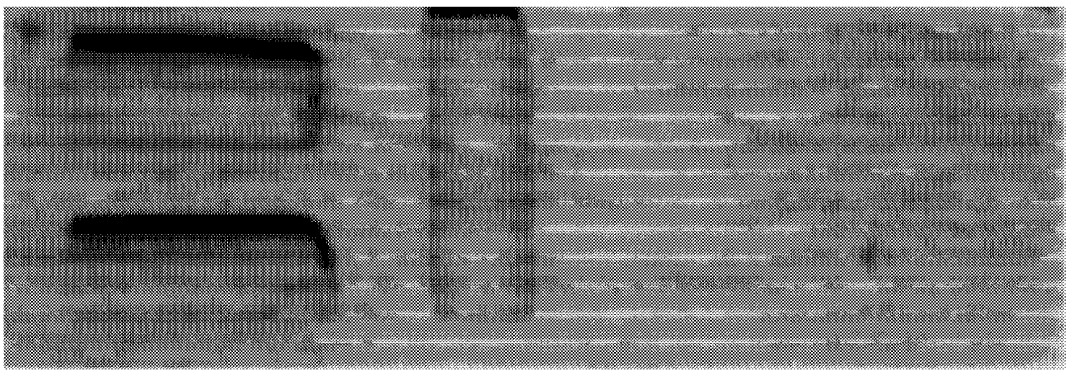

Figure A–15 Photograph of Bluejacket Outcrop Sample Block Showing the Relative Positions of the Vertical (Perpendicular to Laminations) and Horizontal (Parallel to Laminations) Plugs used for Capillary Pressure and Relative Permeability Measurements.

A.1.2.5 Spontaneous Imbibition

CT scanning was used to measure saturation distribution in a core plug during spontaneous imbibition. The 3/4 in. diameter plugs were cut parallel to the laminations. To allow fluids access only through one end, the plug was encapsulated around the circumferences with Castolite resin. The plug was first saturated with brine; next, a centrifuge drainage and dynamic drainage were used to bring it to 65% oil saturation. At residual brine saturation condition, it displays a strong contrast in saturation between the higher porosity/permeability regions and the low porosity/permeability ripples. In Figure A–16, the brine advancement in the plug is shown. In Figure A–17, the oil production as a function of time is shown. This test indicates that, for this strongly water wet sandstone, the majority of the movable oil (25% of the pore volume) can be removed by spontaneous imbibition without the need for any external driving potential.

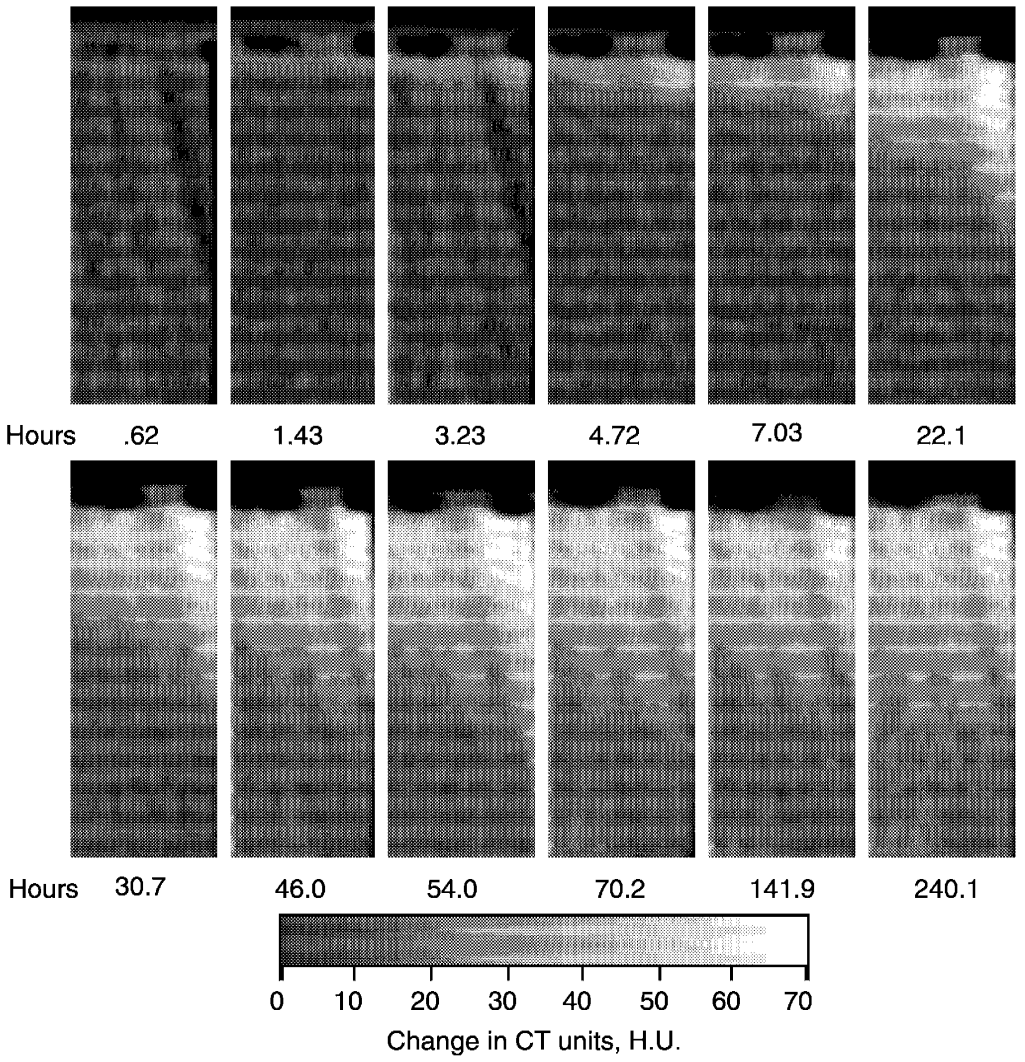

Figure A–16 Brine (Lighter Color) Advancement into the Bartlesville Sand Core Plug During Spontaneous Imbibition Test.

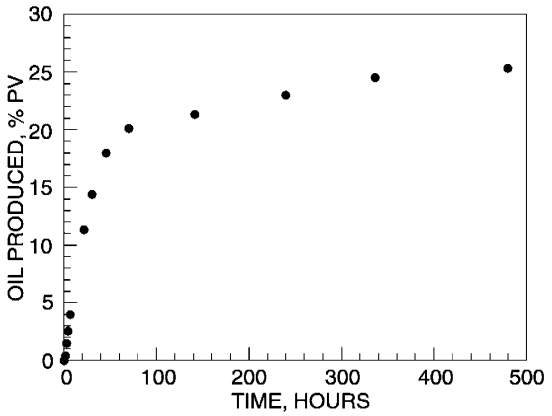

Figure A–17 Oil Production During Spontaneous Imbibition Test of Bartlesville Sand Plug.

A.2 Vertical Sample CT Scanner

Vertical fluid flow in reservoirs can be modeled in the laboratory by using vertical core samples, as these are the cores actually recovered from the reservoirs. To study this process, a CT scanner for vertical core holders has been acquired. Input from research and facilities management was incorporated into planning the installation of the vertical core CT scanner in a number of working meetings that were held in January and February. A laboratory will be constructed in the present Mobile Laboratory located in Building 1, with the ceiling height designed for easy access to the lighting and air conditioning facility. The plan allows for efficient use of two CT scanners operating in adjacent rooms and easy access between the control rooms. A sample preparation laboratory with easy access to both the core-cutting area and CT scanners is included in the plan. This laboratory will ensure efficient use of the scanners by reducing the time needed in the CT laboratory to set up experiments for scanning. This will permit a rapid turnaround time in performing CT scans as part of various research projects. The floor plan also ensures the needed space for moving large equipment components when repair or

replacement is needed. Safety in handling large cores for the vertical scanner has been addressed by providing a mechanical lift in the pit below the vertical scanner and adequate access limiting barriers. The support and vertical movement of the core is provided by a support table driven by a stepping motor. For increased safety, the motor and the controllers will be situated in the pit to facilitate installation, maintenance, and repair. Architectural design is in progress, and a mechanical engineering consultant will be hired for the design of the sample table.

A.3 Upscaling Methods

A.3.1 Renormalization

In Task 1, various upscaling methods described in literature, including renormalization, have been coded in a computer program. The renormalization method allows the calculation of effective permeability of groups of 2 x 2 grid blocks. The renormalization approach used here, based on the original method described by King,[1] calculates: (1) the flow through the pairs with permeability values K_{11}, K_{12} and K_{21}, K_{22}; (2) the flow through the pairs with the permeabilities K_T and K_B; and (3) the flow through the block with the effective permeability K_{RN} (Fig. A–18). Figure A–19 is shows a grid system with 49 x 32 cells which is reduced successively by renormalization to 24 x 16, 12 x 8, 6 x 4, and 3 x 2 based on one of the permeability distributions of the ripple-bedded Bartlesville sand sample determined by minipermeameter measurements. Also shown in Figure A–19 are the simulation results of a tracer flowing through these different renormalized permeability configurations after 0.4 PV of tracer have been injected. The tracer front movement is adequately preserved down to the 12 x 8 grid, which is coarsened by a factor of 4 on each axis corresponding to a total reduction in the number of grid blocks by a factor of 16. This shows that the renormalization approach preserves the system's main permeability features. In Figures A–20 to A–24, the detailed results of the tracer simulations for various renormalization levels are shown. In Figure A–20, the maximum available information is used, showing simulations on the 49 x 32 gridding, at 0.2 PV tracer injected intervals, with the flow from left to right. Each grid block permeability value is the value generated by minipermeameter measurement. Due to permeability contrasts, detailed fingering, is observed, with the breakthrough in the high permeability layer next to the top of the sample and significant lagging of the tracer in the low permeability lower layers. In Figures A–21 to A–24, simulations performed on renormalized permeability distributions are shown. The tracer distribution is shown at successive 0.2 PV tracer injected intervals, with the flow from left to right. In the left column, the simulations are performed on the coarse renormalized grid; thus, the results of the simulations are affected by both changes in permeability values and grid size. In the right column are the results of simulations in which the grid size is kept constant at 48 x 32, to eliminate the effect of grid size variation. The 48 x 32 grid is obtained by replacing each of the coarse renormalized grid blocks with the appropriate number of fine grid blocks, each with a permeability value equal to the value of the renormalized grid block on which it falls. Thus the 24 x 16 fine grid will contain 48 x 32 total grid cells, generated by replacing each of the coarse 24 x 16 grid cells by 2 x 2 cells each having a permeability value equal to the cell they replaced. The coarse grid simulations preserve very well the permeability and the tracer

flow patterns down to the 12 x 8 renormalization level. The fine grid simulations show that even down to the 6 x 4 renormalization level, the general permeability and tracer flow patterns are preserved. In Figure A–25, the cumulative tracer production is displayed as a function of time for the various simulations. In agreement with the results shown in Figures A–20 to A–24, the production curves show very strong overlap down to the 12 x 8 level for coarse grid and 6 x 4 level for fine grid. A significant shift in the curves is noticed for the 6 x 4 coarse grid, both coarse and fine grid 3 x 2 case and the 1 x 1(homogeneous, fine grid) case. The shift is due either to the permeability distribution, which significantly alters the flow pattern by replacing the fingering with a piston-like front movement, or to numerical dispersion in the coarse grid case.

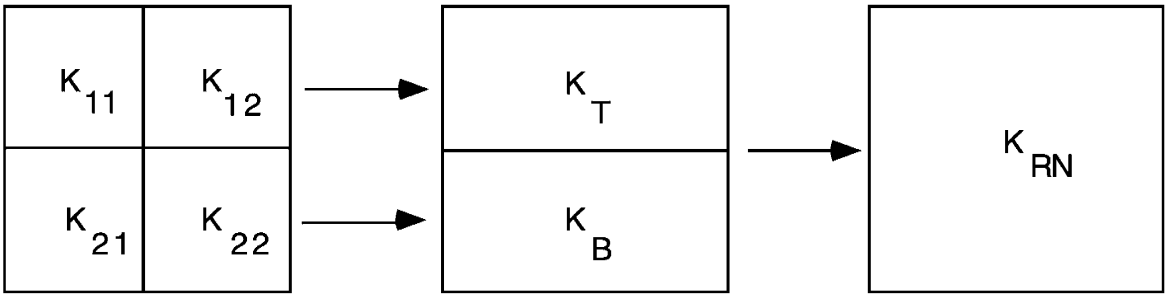

$$K_T = \frac{K_{11} * K_{12}}{K_{11} + K_{12}} \qquad K_B = \frac{K_{21} * K_{22}}{K_{21} + K_{22}} \qquad K_{RN} = K_T + K_B$$

Figure A–18 Renormalization Method Intermediate Steps

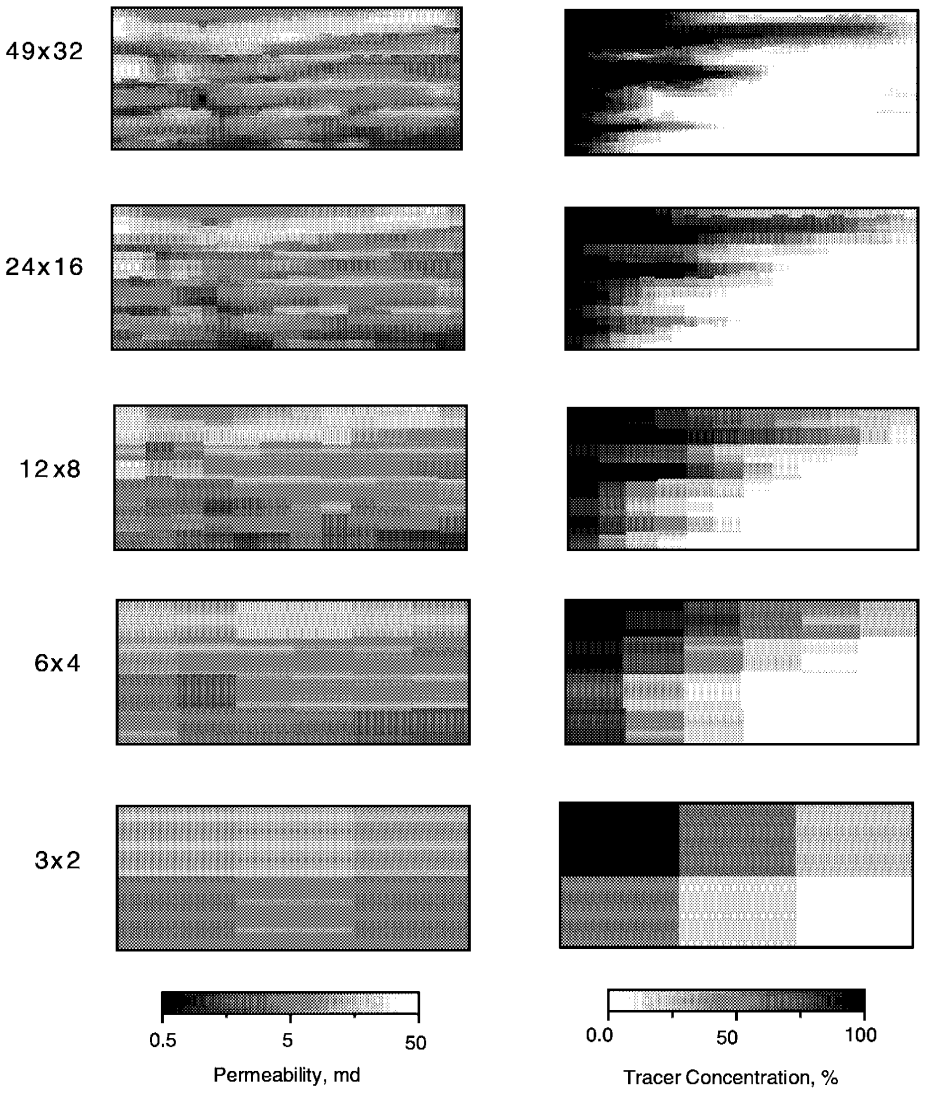

Figure A–19 **Renormalized Permeability Distribution (left) and Corresponding Tracer Simulation after 0.4 PV Tracer Injecting from Left End (right). Grid dimensions are indicated in the first column.**

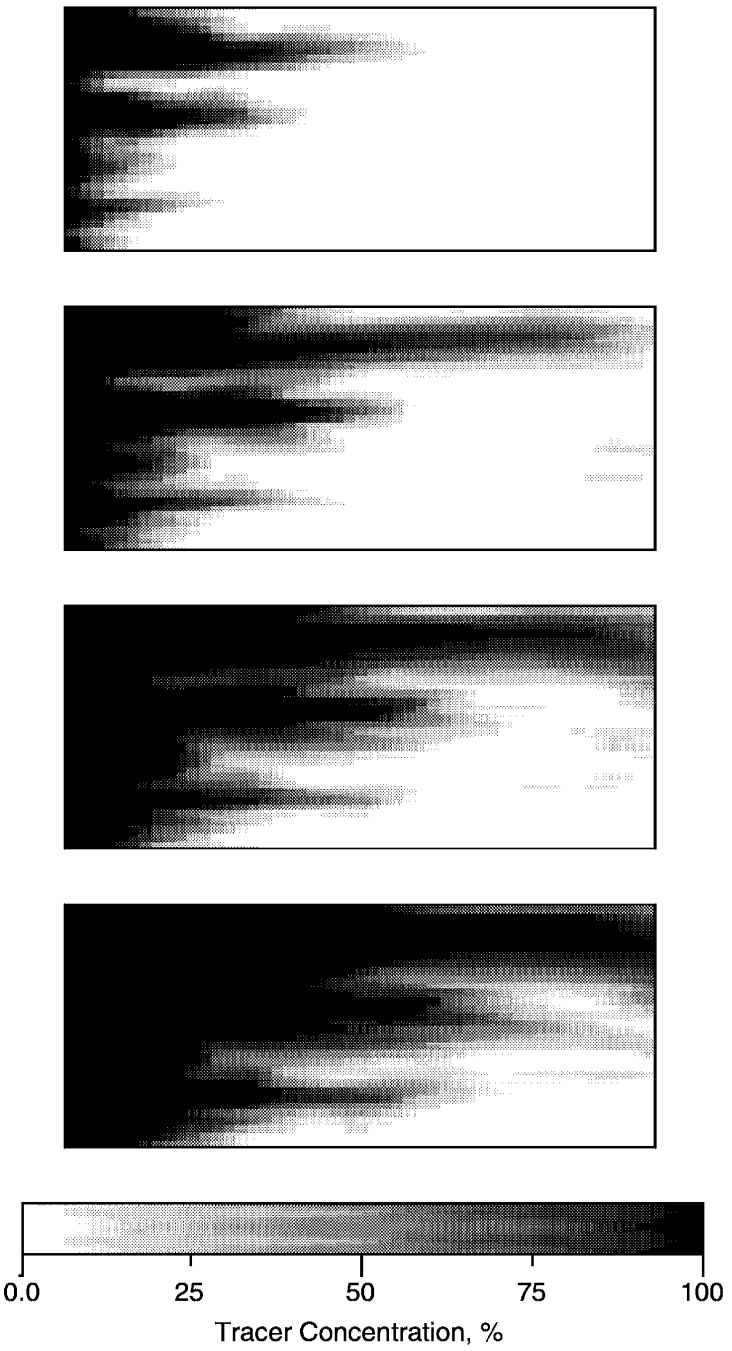

Figure A–20 Flow Simulations for 49 x 32 Grid at 0.2 PV Injected Fluid Increments. Flow is from left to right.

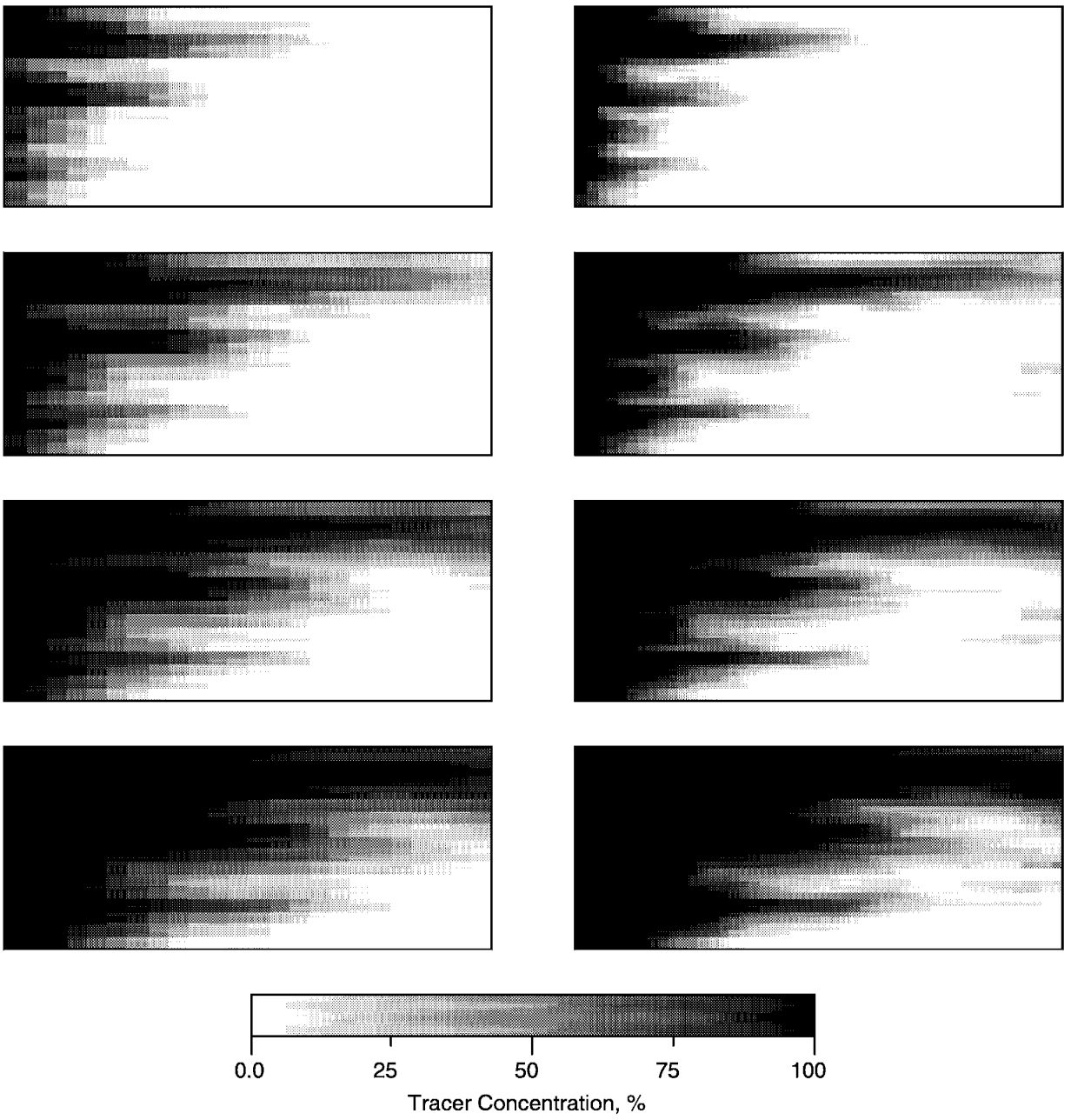

Figure A–21 **Flow Simulations for 24 x 16 Permeability Distribution at 0.2 PV Injected Fluid Increments. At left, the simulation is performed with a 24 x 16 grid. At right, the simulation is performed for the same permeability distribution, but with a 48 x 32 grid.**

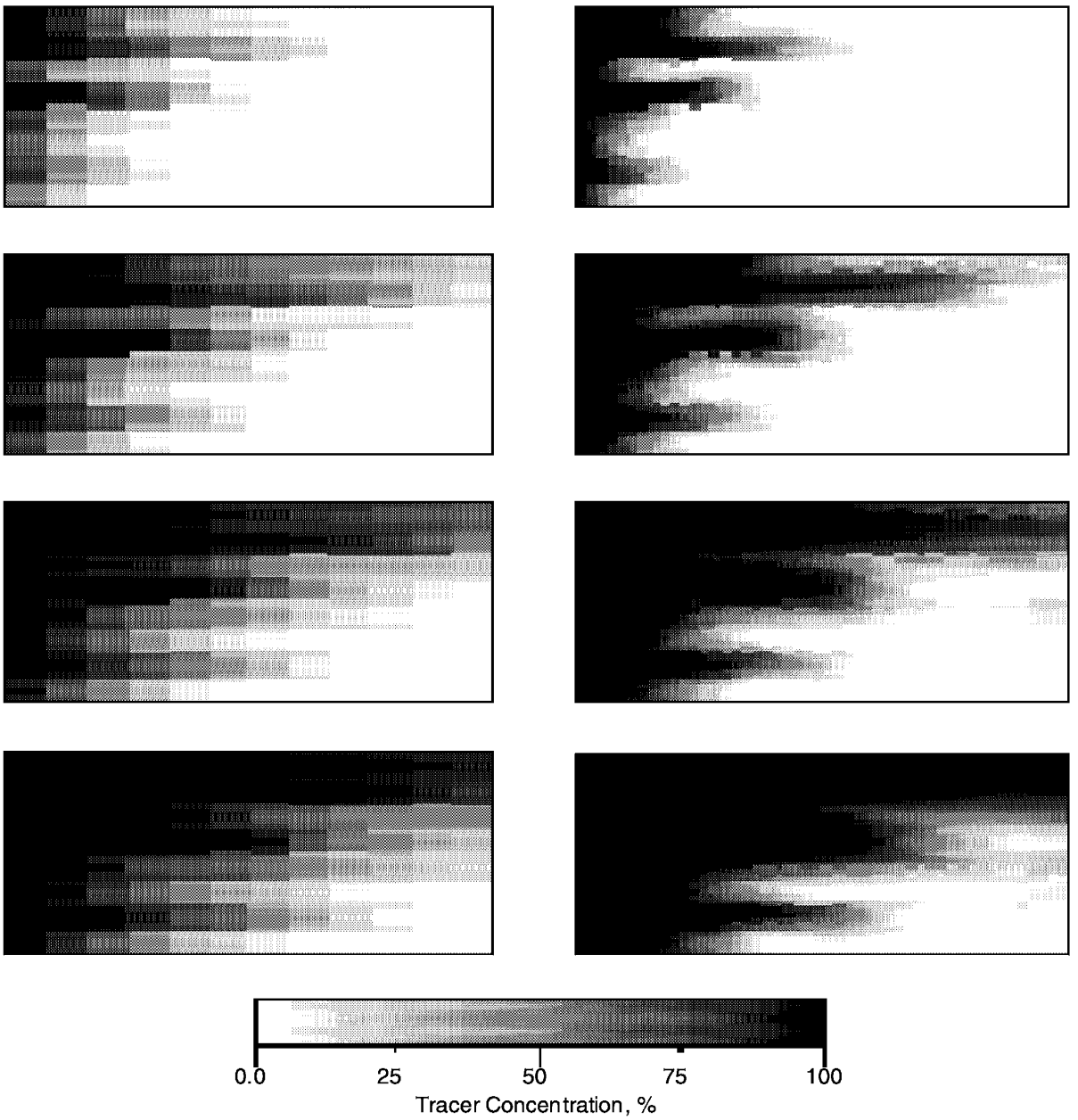

Figure A–22 **Flow Simulations for 12 x 8 Permeability Distribution at 0.2 PV Injected Fluid Increments. At left, the simulation is performed with a 12 x 8 grid. At right, the simulation is performed for the same permeability distribution, but with a 48 x 32 grid.**

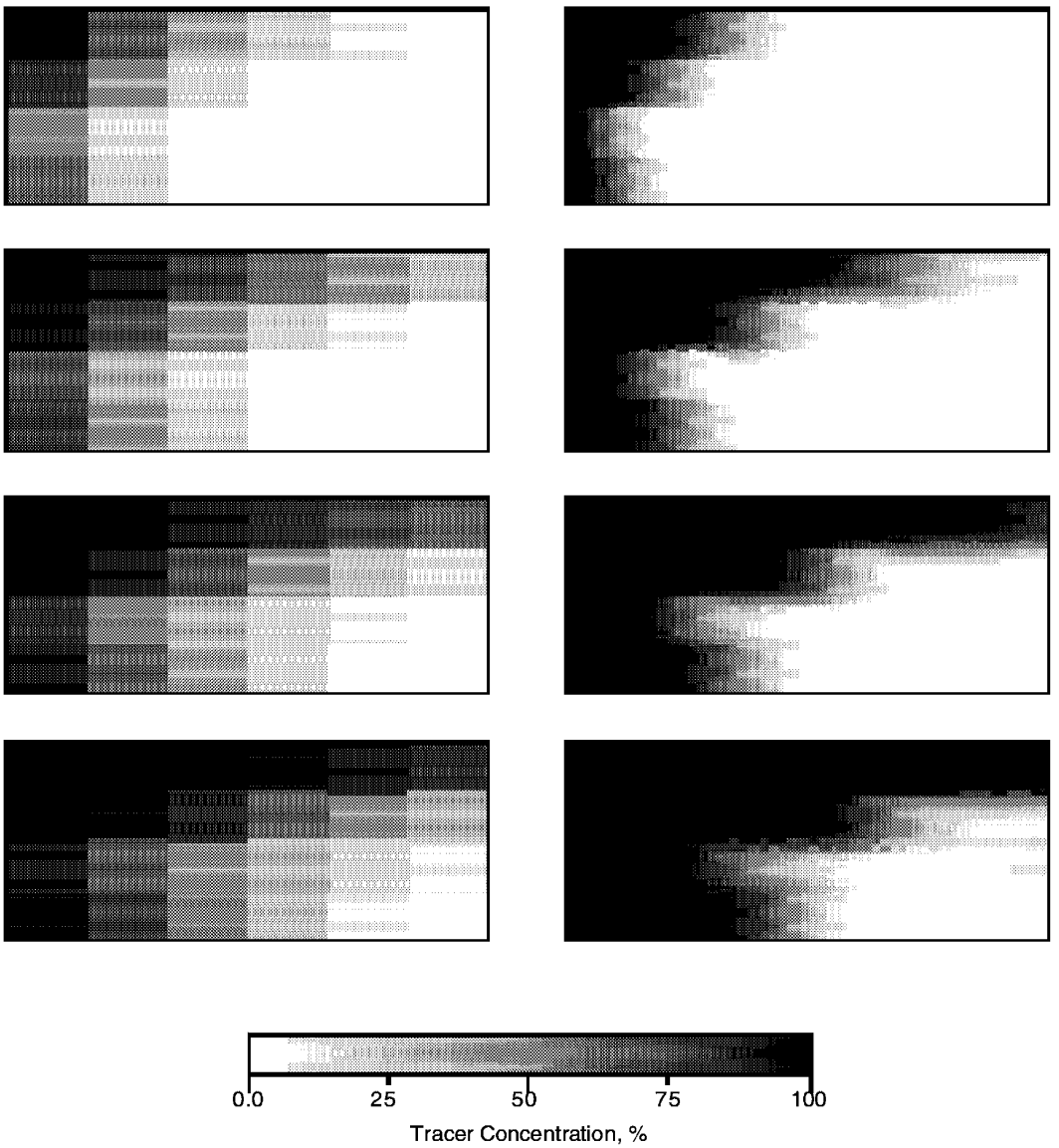

Figure A–23 **Flow Simulations for 6 x 4 Permeability Distribution at 0.2 PV Injected Fluid Increments. At left, the simulation is performed with a 6 x 4 grid. At right, the simulation is performed for the same permeability distribution, but with a 48 x 32 grid.**

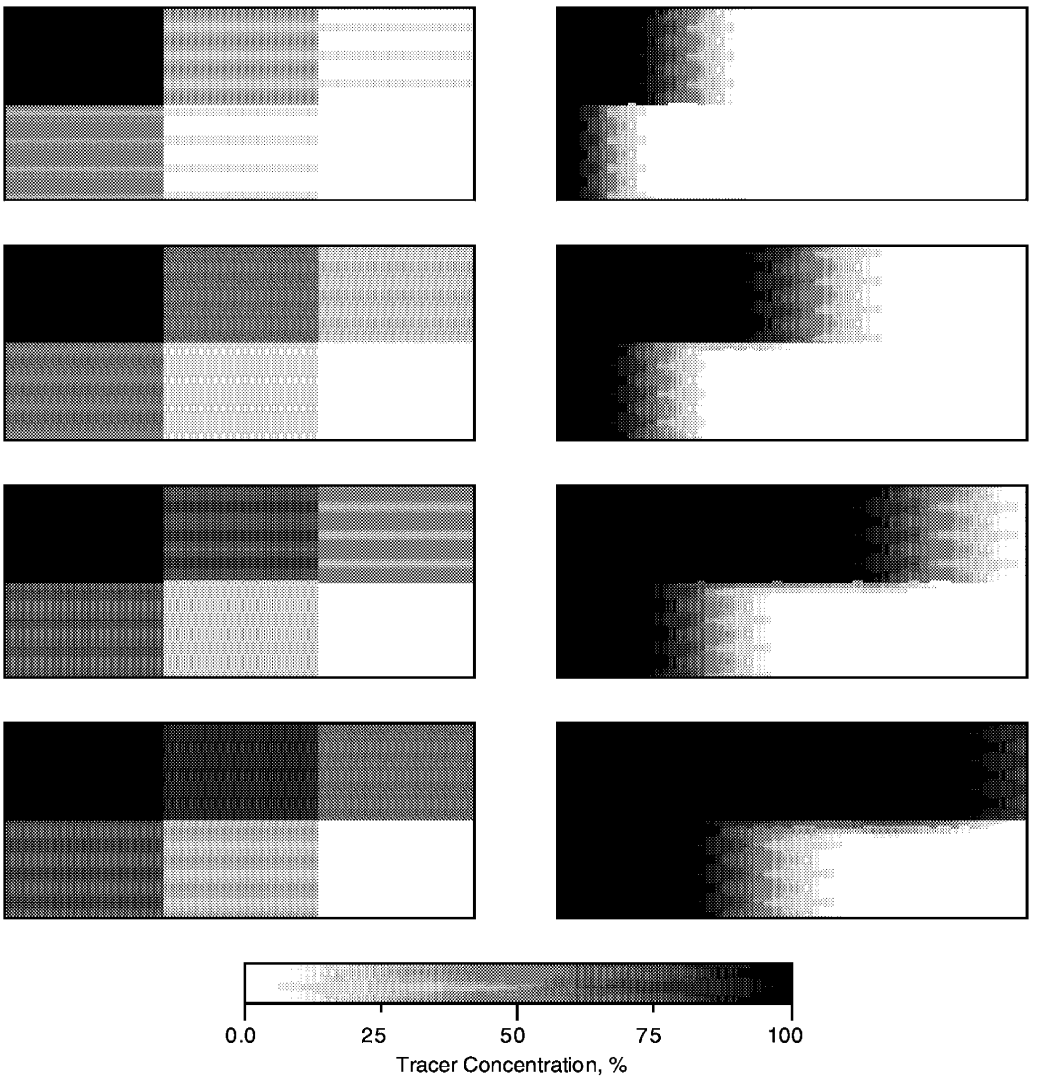

Figure A–24 **Flow Simulations for 3 x 2 Permeability Distribution at 0.2 PV Injected Fluid Increments. At left, the simulation is performed with a 3 x 2 grid. At right, the simulation is performed for the same permeability distribution, but with a 48 x 32 grid.**

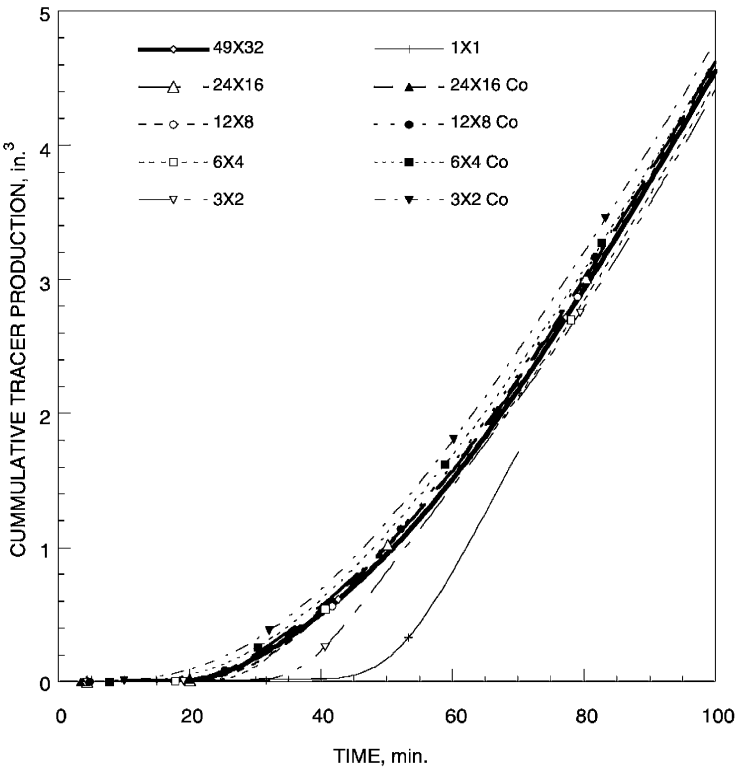

Figure A–25 Cumulative Production as a Function of Injection Time. Each line corresponds to a certain grid size. The symbols containing CO in their names correspond to the respective coarse grid patterns, while all other symbols correspond to a 48 x 32 grid pattern, except the initial 49 x 32 grid pattern.

A.3.2 Effective Permeability Tensor

Computational costs limit large-scale reservoir simulations to coarse grid systems. Determination of an effective permeability for a grid block requires a correct scaleup of small-scale permeabilities measured on core samples. Conventional scaleup techniques are limited to a diagonal tensor representation of effective permeability. Therefore, such techniques cannot handle crossflow effects exemplified by crossbedded permeability structures that may be present on a smaller scale. The analytical method developed at the University of Tulsa (TU) (Aasum, et al. 1993; Kasap and Lake 1990) was used to perform preliminary calculations of the effective permeability tensor for the Bartlesville and Tallant sandstones.

A full permeability tensor is required to correctly preserve flow-diverting effects in the cases where permeability heterogeneities generate a pressure drop transverse to the direction of applied pressure drop. In the following two examples, the applied pressure drop is along the horizontal axis.

- Laminated permeability structures are anisotropic and oriented at angles other than those parallel and perpendicular to the simulation coordinate axes (general anisotropy). An example is shown in Figure A–26.
- Structures are distributed asymmetrically. An example of this is shown in Figure A–27.

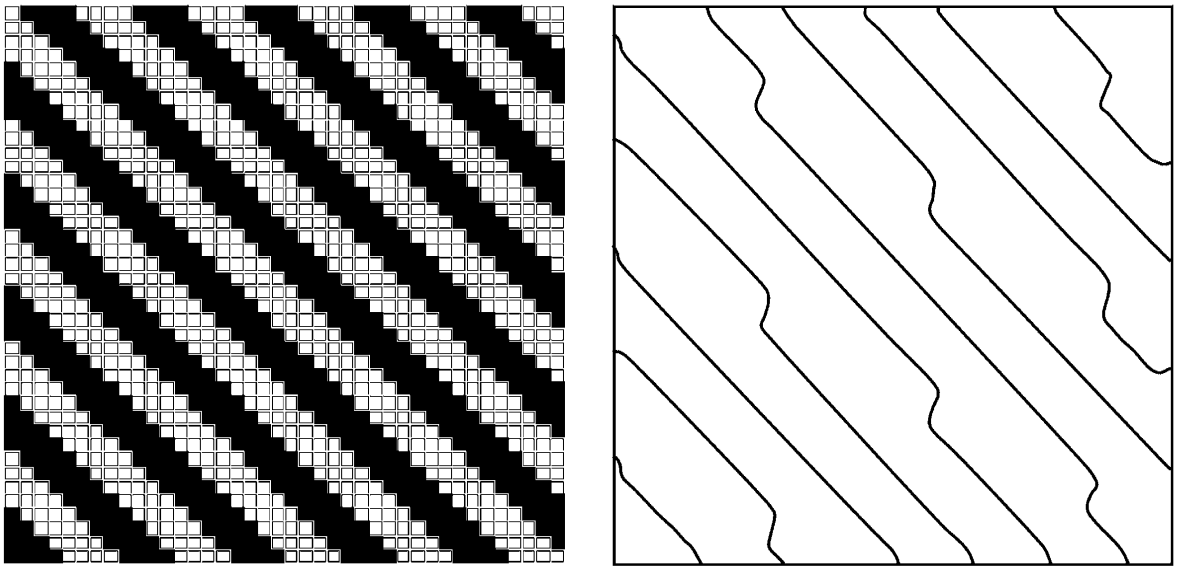

Figure A–26 Crossbedding Creates Crossflow and Transverse Pressure Gradient. *A*, Synthetic crossbedding: dark 20 md, light 1,000 md; *B*, isopotential lines during a flow from left to right, indicating crossflow from bottom to top supported by transverse pressure gradient.

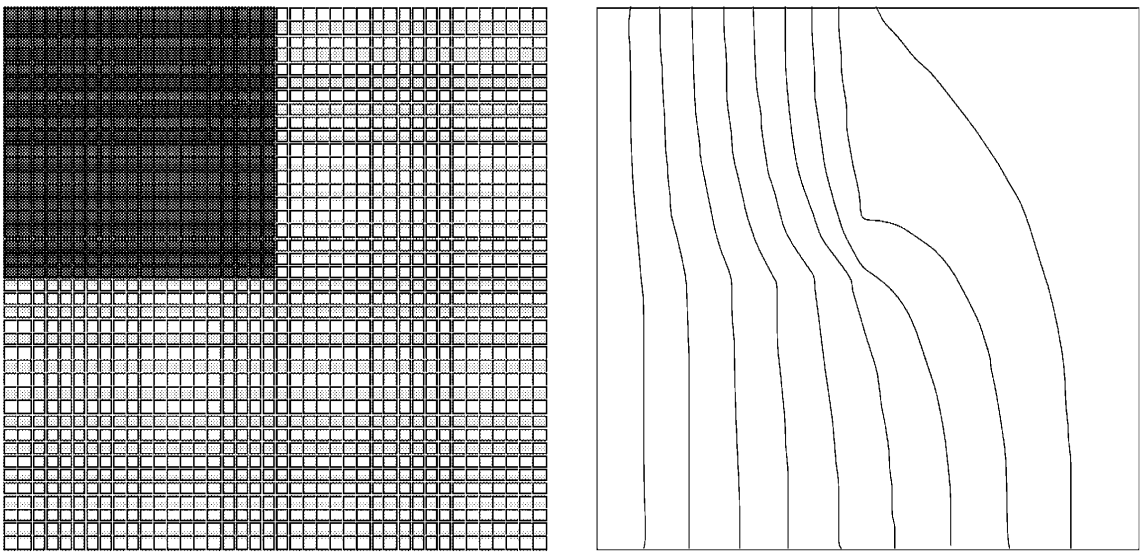

(a) (b)

Figure A–27 Asymmetric Heterogeneity Creates Crossflow and Transverse Pressure Gradient. *A*, Synthetic heterogeneity: dark 1 md, light 1,000 md; *B*, isopotential lines during a flow from left to right, indicating crossflow from bottom to top supported by transverse pressure gradient.

There are three steps involved in generating an effective permeability tensor:

1. Determine the permeabilities along the principal directions.

   Divide the grid block with small scale isotropic permeability heterogeneities into four quadrants. Determine the principal permeability directions by identifying the two normal directions which yield the maximum permeability contrast.

2. Calculate the effective permeability tensor in each quadrant by performing coordinate rotation.

   The permeabilities in the principal directions k'_{ii} and the orientation angle α are determined in Step 1. These parameters are used in a coordinate rotation procedure which yields the following effective permeability tensor elements along the simulation coordinate axes:

$$k_{xx} = (\cos\alpha)^2 k'_{xx} + (\sin\alpha)^2 k'_{yy} \tag{A–1}$$

$$k_{xy} = \sin\alpha\cos\alpha\left(k'_{xx} - k'_{yy}\right) \tag{A–2}$$

$$k_{yx} = \sin\alpha\cos\alpha\left(k'_{xx} - k'_{yy}\right) \tag{A–3}$$

$$k_{yy} = (\sin\alpha)^2 k'_{xx} + (\cos\alpha)^2 k'_{yy} \tag{A–4}$$

At this point an effective permeability tensor has been determined for each of the four quadrants. The final step is to calculate the effective permeability tensor for the entire permeability field. Steps 1 and 2 could conceivably be performed on the complete permeability field.

3. Calculate the effective permeability tensor elements for the entire system.

   The elements of the effective permeability tensor $\tilde{k}_{ii}$ are obtained from the following expressions:

$$\tilde{k}_{xx} = \frac{\tilde{k}_{x_{app}}}{1 - \left(\left[\left(\frac{\partial \tilde{p}}{\partial x} \right)_Y \Big/ \left(\frac{\partial \tilde{p}}{\partial y} \right)_Y \right] \times \left[\left(\frac{\partial \tilde{p}}{\partial y} \right)_X \Big/ \left(\frac{\partial \tilde{p}}{\partial x} \right)_X \right] \right)} \tag{A–5}$$

$$\tilde{k}_{xy} = -\tilde{k}_{xx} \left(\frac{\partial \tilde{p}}{\partial x} \right)_Y \Big/ \left(\frac{\partial \tilde{p}}{\partial y} \right)_Y \tag{A–6}$$

   Where the ~ symbol indicates averages, *"app"* means apparent, and subscripts indicate flow direction.

   The *y*-direction permeabilities are calculated similarly. The subscripts on pressure gradients indicate main flow directions, and

$$\ddot{k}_{xapp} = \left(k_{xx} - \frac{k_{xy}^2}{k_{yy}} \right) \tag{A–7}$$

The method is being used to calculate the effective permeability tensor for Tallant sandstone core. Complex small-scale heterogeneities, such as crossflow within the homogenized sub volumes, can be taken into account by the model. Preliminary calculations indicate that the ripples present in the sample allow only a relatively small crossflow. To enhance the crossflow effect, an experiment needs to be performed within a block with the laminations orientation at a higher angle with respect to the main flow direction.

The analytical and numerical effective permeability calculation techniques are compared. Both methods calculate effective permeability as a 2D tensor because the measured data were in 2D. In general, the positive *x*-direction is in the right direction when facing the 2D plane, and the positive *y*-direction is the direction normal to the *x*-direction at 90° when rotating counter-clockwise. The calculated tensors are in the form

$$k_{\text{mod } elrock} = \begin{bmatrix} k_{xx} & k_{xy} \\ k_{yx} & k_{yy} \end{bmatrix} \tag{A–8}$$

Tallant Sandstone: The analytical tensor method was applied to calculate the effective permeability of Tallant sandstone using the CT and probe minipermeameter data. Numerical flow simulations were run to calculate the effective permeability tensor and to compare with the results of the analytical method. The comparison indicates an excellent match between analytical and numerical simulations.

$$k_{numtal} = \begin{bmatrix} 187.3 & 1.1 \\ 0.4 & 202.4 \end{bmatrix} \tag{A–9}$$

$$k_{antal} = \begin{bmatrix} 188.7 & -10.2 \\ -0.5 & 200.8 \end{bmatrix} \tag{A–10}$$

Both analytical (k_{antal}) and numerical (k_{numtal}) tensor permeabilities indicate that small permeability anisotropy is created by the ripples. The calculated effective permeabilities both numerically and analytically in the x- and y-directions compare well with the measured permeability of 210 md.

Bluejacket Sandstone: Detailed probe minipermeameter data for a Bluejacket sandstone sample were used to calculate its effective permeability tensor and anisotropy ratio. Probe permeameter measurements were conducted on the six faces of the cut sample (Fig. A–28). Analytical ($k_{anbj}1$) and flow simulations ($k_{nubj}1$) results are shown below for faces 1, 2, and 4 of the six block faces:

$$k_{nubj1} = \begin{bmatrix} 9.4 & -0.02 \\ 0.05 & 4.7 \end{bmatrix} \tag{A–11}$$

$$k_{anbj1} = \begin{bmatrix} 8.8 & 0.3 \\ 0.5 & 5.3 \end{bmatrix} \tag{A–12}$$

$$k_{nubj2} = \begin{bmatrix} 8.6 & -0.00 \\ -0.00 & 8.5 \end{bmatrix} \tag{A–13}$$

$$k_{anbj2} = \begin{bmatrix} 8.2 & -0.01 \\ -0.00 & 8.9 \end{bmatrix} \tag{A–14}$$

$$k_{nubj4} = \begin{bmatrix} 3.2 & 0.04 \\ -0.00 & 4.7 \end{bmatrix} \quad \text{(A–17)}$$

$$k_{anbj4} = \begin{bmatrix} 3.3 & 0.14 \\ 0.14 & 4.7 \end{bmatrix} \quad \text{(A–18)}$$

Similar results have been obtained for the faces 3, 5, and 6.

The above results indicate that the Bluejacket sandstone sample was cut almost parallel to the bedding plane. Two faces (2 and 5) that are parallel to the bedding plane (top and bottom faces in this case) indeed show no anisotropy. All other faces show anisotropy with a constant anisotropy ratio of 1.5–2. The only exception to this is face 6, where the anisotropy ratio goes up to 3.5.

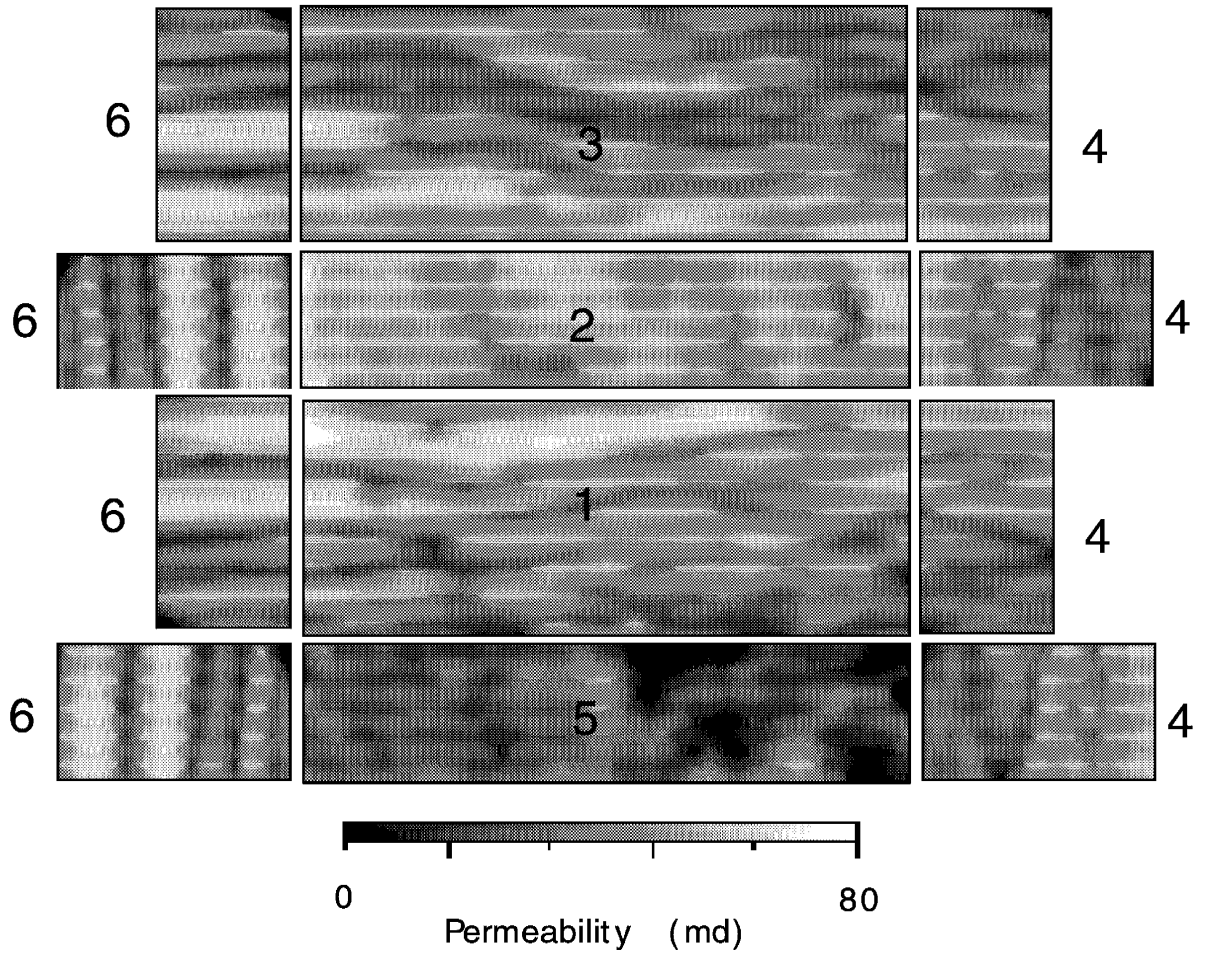

Figure A–28 Permeability Distribution Measured by Probe Minipermeameter for the Six Sides of the Bartlesville Block

A.4 SUMMARY

Improvements in minipermeameter measurements allowed to produce detailed permeability maps to characterize the permeability contrasts in the ripple-bedded Bartlesville (Bluejacket) sandstone sample selected.

Good agreement has been observed between CT and NMR measurements of porosity for the Bartlesville block.

Permeability-Porosity Correlations, generated by both CT minipermeameter and PIA, show agreement. They will be used together with CT porosity to calculate the 3D permeability distribution within the Bartlesville sandstone block.

A new approach to saturate low-permeability rock blocks encapsulated in epoxy has been designed. It allows the use of larger injection pressures by placing the epoxied sample in a core holder and applying overburden pressure.

The effect of end piece design has been tested by simulations. Those indicated that the three-compartment design does not introduce undesired channeling, but does allow the monitoring of flow in regions of different permeabilities.

Spontaneous imbibition on a Bartlesville sandstone plug indicates complete removal of the movable oil due only to capillary forces.

Plans have been completed for installation of a vertical sample CT scanner, which will allow study of vertical drainage in samples (such as the ripple-bedded Bartlesville sandstone (studied) that have significant vertical flow barriers.

Two single-phase upscaling methods have been tested using the permeability data for the Bartlesville slab. The renormalization method indicates that a grid as coarse as 12 x 8 adequately preserves the flow pattern. The effective permeability tensor calculations indicate a small crossflow effect due to the essentially horizontal placement of permeability heterogeneity. It indicates the tensor effect is very small for this sample in describing effective permeability.